377 MSG/SCOK (FOIA Manager)   23 July 2015
2051 Wyoming Blvd., S.E.
Kirtland AFB NM 87117-5607

John Greenewald

Dear Mr. Greenewald,

This response is considered a full response to the records you requested on 15 April 15 under
FOIA Case #2015-03511-F received by this office 15 April 15 for "Title: (U) Autonomous
Quality Space Imagery for LEO/GEO Space Situation Awareness PDF URL: (pdf) - 2 MB -
Accession Number: ADB371291 Personal Author(s): Geller, David K Corporate Author: UTAH
STATE UNIV LOGAN Report Date: 28 Jun 2011 Descriptive Note: Final rept. 16 May 2008-4
Apr 2011 Pages:51 Page(s) Report Number: AFRL-RV-PS - TR-2011-0070 AFRL-RV-PS (
AFRLRVPSTR20110070 AFRLRVPS), XC - TR-2011-0070 AFRL-RV-PS (XCTR20110070
AFRLRVPS) Monitor Series: TR-2011-0070 (TR20110070) , AFRL-RV-PS (AFRLRVPS)
Contract/Grant/Transfer Number: FA9453-08-C-0164 (FA945308C0164)". If you interpret this
response as not fully complying with your request, you may contact the undersigned to help
resolve your concerns.

You may also formally appeal this response if you consider it an adverse action by writing to the
Office of the Secretary of the Air Force. Your appeal should be postmarked no later than 60
calendar days from the date of this letter. Please address your letter as follows:

    Secretary of the Air Force
    THRU: 377 MSG/SCOK (FOIA Manager)
    2051 Wyoming Blvd., S.E.
    Kirtland AFB NM 87117-5607

                    Sincerely,

                    DANNY O. OGAS, DAFC, USAF
                    Freedom of Information Act Manager

The following notice applies to any unclassified (including originally classified and now declassified) technical reports released to "qualified U.S. contractors" under the provisions of DoD Directive 5230.25, Withholding of Unclassified Technical Data From Public Disclosure.

<u>**NOTICE TO ACCOMPANY THE DISSEMINATION OF EXPORT-CONTROLLED TECHNICAL DATA**</u>

1. Export of information contained herein, which includes, in some circumstances, release to foreign nationals within the United States, without first obtaining approval or license from the Department of State for items controlled by the International Traffic in Arms Regulations (ITAR), or the Department of Commerce for items controlled by the Export Administration Regulations (EAR), may constitute a violation of law.

2. Under 22 U.S.C. 2778 the penalty for unlawful export of items or information controlled under the ITAR is up to ten years imprisonment, or a fine of $1,000,000, or both. Under 50 U.S.C., Appendix 2410, the penalty for unlawful export of items or information controlled under the EAR is a fine of up to $1,000,000, or five times the value of the exports, whichever is greater; or for an individual, imprisonment of up to 10 years, or a fine of up to $250,000, or both.

3. In accordance with your certification that establishes you as a "qualified U.S. Contractor", unauthorized dissemination of this information is prohibited and may result in disqualification as a qualified U.S. contractor, and may be considered in determining your eligibility for future contracts with the Department of Defense.

4. The U.S. Government assumes no liability for direct patent infringement, or contributory patent infringement or misuse of technical data.

5. The U.S. Government does not warrant the adequacy, accuracy, currency, or completeness of the technical data.

6. The U.S. Government assumes no liability for loss, damage, or injury resulting from manufacture or use for any purpose of any product, article, system, or material involving reliance upon any or all technical data furnished in response to the request for technical data.

7. If the technical data furnished by the Government will be used for commercial manufacturing or other profit potential, a license for such use may be necessary. Any payments made in support of the request for data do not include or involve any license rights.

8. A copy of this notice shall be provided with any partial or complete reproduction of these data that are provided to qualified U.S. contractors.

<u>**DESTRUCTION NOTICE**</u>

For classified documents, follow the procedure in DoD 5220.22-M, National Industrial Security Program, Operating Manual, Chapter 5, Section 7, or DoD 5200.1-R, Information Security Program Regulation, Chapter 6, Section 7. For unclassified, limited documents, destroy by any method that will prevent disclosure of contents or reconstruction of the document.

AUTONOMOUS QUALITY SPACE IMAGERY FOR LEO/GEO SPACE SITUATION AWARENESS

David K. Geller

Utah State University
2400 Old Main Hill
Logan, UT 84322-0001

28 June 2011

Final Report

AIR FORCE RESEARCH LABORATORY
Space Vehicles Directorate
3550 Aberdeen Ave SE
AIR FORCE MATERIEL COMMAND
KIRTLAND AIR FORCE BASE, NM 87117-5776

NOTICE AND SIGNATURE PAGE

Qualified requestors may obtain copies of this report from the Defense Technical Information Center (DTIC) (http://www.dtic.mil).

AFRL-RV-PS-TR-2011-0070 HAS BEEN REVIEWED AND IS APPROVED FOR PUBLICATION IN ACCORDANCE WITH ASSIGNED DISTRIBUTION STATEMENT

FRANK CHAVEZ
Program Manager

BRETT J. DEBLONK, Ph.D.
Technical Advisor, Spacecraft Component Technology Branch

B. SINGARAJU, Ph.D.
Deputy Chief, Spacecraft Technology Division
Space Vehicles Directorate

REPORT DOCUMENTATION PAGE

1. REPORT DATE *(DD-MM-YYYY)*	2. REPORT TYPE	3. DATES COVERED *(From - To)*
28-06-2011	Final Report	05-16-2008 - 04-04-2011

4. TITLE AND SUBTITLE

Autonomous Quality Space Imagery for LEO/GEO Space Situation Awareness

5a. CONTRACT NUMBER
FA9453-08-C-0164

5b. GRANT NUMBER

5c. PROGRAM ELEMENT NUMBER
63401F

6. AUTHOR(S)
David K. Geller

5d. PROJECT NUMBER
682J

5e. TASK NUMBER

5f. WORK UNIT NUMBER
299294

7. PERFORMING ORGANIZATION NAME(S) AND ADDRESS(ES)

Utah State University
2400 Old Main Hill
Logan, UT 84322-0001

8. PERFORMING ORGANIZATION REPORT NUMBER

9. SPONSORING / MONITORING AGENCY NAME(S) AND ADDRESS(ES)
Air Force Research Laboratory
Space Vehicles Directorate
3550 Aberdeen Ave SE
Kirtland AFB, NM 87117-5776

10. SPONSOR/MONITOR'S ACRONYM(S)
AFRL/RVSV

11. SPONSOR/MONITOR'S REPORT NUMBER(S)
AFRL-RV-PS-TR-2011-0070

12. DISTRIBUTION / AVAILABILITY STATEMENT
Distribution authorized to U.S. Government agencies and their contractors; Critical Technology; 28 June 2011. Other requests for this document shall be referred to AFRL/RVSV, 3550 Aberdeen Avenue SE, Kirtland AFB, NM 87117-5776.

13. SUPPLEMENTARY NOTES

14. ABSTRACT
Quality space imagery is required for many new and innovative Low Earth Orbit (LEO)/Geosynchronous Orbit (GEO) missions including satellite inspection, servicing, and docking, as well as for general space situational awareness. Current space imagery capabilities require "experts" to be on-site at a mission operation center to conduct image data analysis, mission re-planning, system analysis, and space vehicle commanding. This requires a significant amount of time and money as well as additional delays waiting for downlink/uplink opportunities. The goal of this effort is to move towards a more autonomous approach to collecting quality space imagery by developing autonomous image analysis and mission planning capabilities that can be implemented onboard the space vehicle. The will reduce the required time and effort of the mission operations centers, reduce dependence on downlink/uplink opportunities, and provide space vehicles that can be more responsive to customer input.

15. SUBJECT TERMS
Satellite Inspection, Angles-Only Navigation, Image Processing

16. SECURITY CLASSIFICATION OF:			17. LIMITATION OF ABSTRACT	18. NUMBER OF PAGES	19a. NAME OF RESPONSIBLE PERSON
a. REPORT	**b. ABSTRACT**	**c. THIS PAGE**	SAR	50	Frank Chavez
Unclassified	Unclassified	Unclassified			**19b. TELEPHONE NUMBER** *(include area code)* (505)846-6066

(This page intentionally left blank)

LIST OF FIGURES

List of Figures

1   SUMMARY

This research encompassed a wide range of issues concerning autonomous quality space imagery for LEO and/or GEO operations including a) basic mission planning strategies and techniques to collect quality space images autonomously, b) optimal inspection of satellites ensuring lighting and views from all sides, c) automated image change detection, d) angles-only navigation for orbital proximity operations and satellite inspection, and e) procedures for determining collision probability during orbital proximity operations and satellite inspection.

To obtain high quality images, this study develops methods for automatically inspecting satellites at high resolution and low recurring cost. It does so by first providing basic mission planning concepts and estimating fuel expenditures. Then it provides methods to plan measurements so that the images have good lighting and contain views of all pertinent sides. Next, it examines methods to automatically analyze these images to determine when changes have occurred, possibly warranting further investigation. Next an assessment of angles-only relative orbital navigation is made, since this could be a key Guidance, Navigation, and Control (GN&C) component of a satellite inspection mission, and finally a very unique and specialized algorithm was developed to determine collision probabilities when one spacecraft is in proximity of another spacecraft.

1.1   Basic Mission Planning for LEO/GEO Space Operations

Two key components of mission and trajectory planning are 1) computing Δv required to station-keep at a desired sun-angle and distance from the object i.e. the Δv required for inertial station-keeping and 2) the calculation of optimal maneuvers for proximity operations. Both of these are addressed in this research. Station-keeping Δv is presented as a function of sun-angle, distance from the space object, and orbit type, LEO, GEO, or Medium Earth Orbit (MEO).   Optimal maneuvers are computed using an elegant semi-analytical optimization technique.

1.2   Optimal Inspection of Satellites Ensuring Lighting and Views of All Sides

This study develops methods for automatically obtaining images of satellites at high resolution and low recurring cost by using observer satellites whose combined orbits collectively have excellent views of space objects. It formulates observation of Resident Space Objects (RSOs) by a set of Observer satellites as a convex linear program. Thus global optimality, high speed, and convergence to the optimum are assured. New metrics for predicting the quality of an image taken between two orbiting objects are developed for inclusion into the optimal planning process. The final quality metric contains four terms: (1) predicting diffraction induced blur; (2) ensuring that there is a clear line-of-sight between the objects; (3) ensuring the RSO is illuminated; (4) evaluating the lighting angle. In addition, new methods find an observation strategy guaranteeing that all RSOs are characterized on all of their important sides. The theory is also extended to emphasize the characterization of especially important RSOs, both at particular time intervals and relative to other RSOs. Simulation results confirm the viability of the technique on a variety of orbits.

1

1.3 Change Detection

Once quality images are available, automated visual inspection systems have the potential to improve space situational awareness capabilities. However, satellite inspection systems are subject to harsh lighting conditions and bandwidth constraints which necessitate a unique approach. This study presents two approaches to automated change detection. The first method calculates a planar homography relating two images, so that the viewpoint of one image may be warped to the viewpoint of the other. The second method estimates the pose of the object in the image, so that a synthetic comparison image can be generated from a pre-existing model of the object. Each algorithm is simulated under varying lighting and pose conditions.

1.4 Angles-Only Navigation for Orbital Proximity Operations

Angles-only relative orbital navigation is simple, robust, and well proven in many applications, and may be a key GN&C component for satellite inspection missions. However, it is sometimes ill-conditioned for orbital rendezvous and proximity operations because, without a direct range measurement, the distance to approaching satellites must be estimated by firing thrusters and observing the change in the RSO's bearing. Nevertheless, the simplicity of angles-only navigation gives it great appeal. The viability of this technique for relative navigation is examined by building a high-fidelity simulation including six degree-of-freedom dynamic models, actuator and sensor models, associated attitude and translational controllers, and an angles-only navigation extended Kalman filter. Range observability is evaluated during open and closed-loop proximity operations, similar to a satellite inspection mission.

1.5 Procedure for Determining Collision Probability during Proximity

A procedure to estimate collision probability during orbital proximity operations is developed. The algorithm utilizes a series of metrics that can be placed into two main categories. The first category provides an estimate of the instantaneous probability of collision. This also places an upper bound on the total probability of collision. The second category of metrics provides an estimate of total collision probability. The metrics are arranged in a hierarchy such that those metrics which can be computed quickly are calculated first. As the algorithm progresses the metrics become more costly to compute, but yield more accurate estimates of collision probability.

2 INTRODUCTION

Quality space imagery is required for many new and innovative LEO/GEO missions including satellite inspection, servicing, and docking, as well for general space situational awareness. Current space imagery capabilities require "experts" to be on-site at a Mission Operation Center to conduct image data analysis, mission re-planning, system analysis, and space vehicle commanding. This requires a significant amount time and money as well as additional delays waiting for downlink/uplink opportunities. The goal of this effort is to move towards a more autonomous approach to collecting quality space imagery by developing autonomous image analysis and mission planning capabilities that can be implemented onboard the space vehicle. This will reduce the required time and effort of the Mission Operations Centers, reduce dependence on downlink/uplink opportunities, and provide space vehicles that can be more responsive to customer input.

To obtain high quality images, this study develops methods for automatically inspecting satellites at high resolution and low recurring cost. It does so by first providing basic mission planning concepts and estimating fuel expenditures. Then it provides methods to plan measurements so that the images have good lighting and contain views of all pertinent sides. Next, it examines methods to automatically analyze these images to determine when changes have occurred, possibly warranting further investigation. Finally, an assessment of angles-only relative orbital navigation is made, since this could be a key GN&C component of an inspection mission. The following subsections describe each of these steps.

2.1   Basic Mission Planning for LEO/GEO Space Operations

This study considers two scenarios that cover a wide spectrum of applications. The first is an autonomous survey of an unknown or partially known space object. For this scenario, an optimal trajectory plan would be developed onboard the space vehicle such that a survey of the object could be conducted within desired customer time constraints. During the survey, basic image metrics such as lighting, under/over-exposure, spatial resolution, and contrast are evaluated. Trajectory modifications are made if required, and images are saved and stored for downlink to the ground.

The second scenario has an inspector spacecraft monitoring and evaluating the health of a well known object. In this scenario the objective is to obtain very precise and detailed imagery of the object or a component of the object. Detailed image analysis is conducted onboard the space vehicle and metrics for lighting, contrast, glare, exposure, blurring, resolution, etc, are computed. The metrics are then used to adjust camera settings and to compute a desired space vehicle position and orientation. Onboard mission managers and trajectory planners then determine an optimal and safe sequence of translation and rotational maneuvers, and an autonomous onboard GN&C system can navigate and execute the maneuvers to achieve the desired position and orientation.

Both of these scenarios can be captured in an ideal autonomous quality space imagery system as shown in the conceptual block diagram in Figure 1. The basic components of this system are: 1) the space vehicle inspection camera and its image processing and analysis algorithms needed to assess the quality of an image, 2) the environment and image device parameter selection algorithms that will improve the image quality, 3) the autonomous mission and trajectory planning algorithms to determine optimal and safe maneuver sequences, and 4) the GN&C algorithms required to implement the trajectory commands and mission plan. These four components were presented and discussed in more detail at the AIAA GNC Conference in Honolulu, Hawaii 2009 [1].
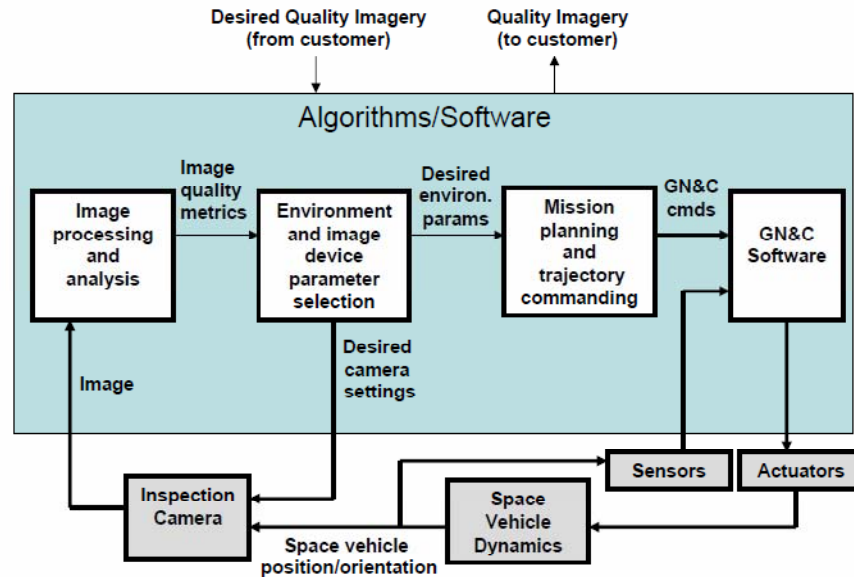
Figure 1. An Ideal Autonomous Quality Space Imagery System

2.2 Optimal Inspection of Satellites Ensuring Lighting and Views of All Sides

To obtain high quality images, this study develops methods for automatically inspecting satellites at high resolution and low recurring cost by using observer satellites whose combined orbits collectively have excellent views of the objects of interest. It formulates observation of Resident Space Objects (RSOs) by a set of Observer satellites as a convex linear program. Thus global optimality, high speed, and convergence to the optimum are assured. New metrics for predicting the quality of an image taken between two orbiting objects are developed for inclusion into the optimal planning process. The final quality metric contains four terms: (1) predicting diffraction induced blur; (2) ensuring that there is a clear line-of-sight between the objects; (3) ensuring the RSO is illuminated; (4) evaluating the lighting angle. In addition, new methods find an observation strategy guaranteeing that all RSOs are inspected on all of their important sides. The theory is also extended to emphasize the inspection of especially important RSOs, both at particular time intervals and relative to other RSOs. Simulation results confirm the viability of the technique on a variety of orbits.

Full details documenting this part of the research were presented at the AIAA GNC Conference in Toronto, August 2010 [2]. This portion of the research was jointly funded by this grant and a grant from the Air Force Office of Scientific Research (AFOSR). The portions of the work devoted to the needs and importance of considering lighting effects and viewpoints of multiple sides are motivated by this grant, while the portions devoted to collectively viewing a large number of RSOs by using a large number of Observers is motivated by the AFOSR grant. A version of these results was prepared also for the IEEE International Conference on Robotics and Automation (ICRA) 2010, but the paper did not finish the public release process in time to be submitted to the ICRA.

2.3 Change Detection

Once images are obtained, they need to be automatically analyzed. Automated visual inspection systems have the potential to improve space situational awareness capabilities. However, satellite inspection systems are subject to harsh lighting conditions and bandwidth constraints which necessitate a unique approach. This study presents two approaches to automated change detection. The first method calculates a planar homography which relates the two images, so that the viewpoint of one image may be warped to the viewpoint of the other. The second method estimates the pose of the object in the image, so that a synthetic comparison image can be generated from a pre-existing model of the object. Each algorithm is simulated under varying lighting and pose conditions. Extended abstracts summarizing these methods have been submitted to the SPIE Conference on Defense, Security, and Sensing ([3], [4]).

An example of these lighting effects is given in Figure 2, an image of the International Space Station taken by a nearby Space Shuttle Mission. Note the dark shadows cast by the body of the station on the center solar arrays, and the bright specular reflections on the round sections of the body.
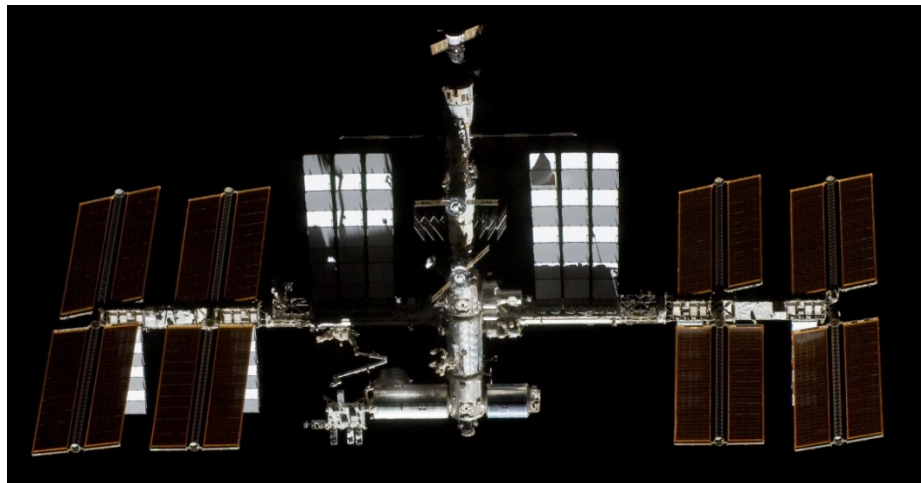
Figure 2. Shadows and Specular Reflections on the International Space Station. Image Credit: NASA S129-E-006396

2.4 Angles-Only Navigation for Orbital Proximity Operations

The intent of this study is to understand the feasibility of Angles-Only Navigation (AON) for satellite inspection missions. One of the simplest yet useful sensors is a simple camera, whether infrared or optical. With a camera, a satellite can track where a second satellite is located within its field-of-view. While such measurements can be obtained from many types of sensors (e.g. Lidar or Radar), the camera has the additional advantage of being entirely passive. Angles-only-navigation can, however, be ill-conditioned for orbital rendezvous and proximity operations because, without a direct range measurement, the distance to approaching satellites must be estimated in other ways. Nevertheless, the simplicity of angles-only navigation gives it great appeal.

Various strategies have been developed to overcome the limitations of AON. Two techniques are 1) taking "apparent diameter" measurements to the RSO, and 2) performing translational maneuvers so the range of the RSO may be estimated. Both methods have their advantages. Apparent diameter measurements are range limited based on the resolution of the camera and require prior knowledge of the satellite being observed. Translational maneuvers consume fuel and shorten the useful life of the satellite.

Translational maneuvers to estimate range have been explored for land and seas based operations, but are not as well understood for orbital proximity operations applications. In concept, a satellite would track its RSO using a camera. The angles-only measurements would be processed by a state estimator like an extended Kalman filter. Assuming the satellite knows where it is, it can narrow the possible locations of the RSO to a narrow cone projecting out from the camera. Of course, the range is unknown at this point. Thrusters can then be fired in a direction that will cause the angle to the RSO to change. This change is a function of the magnitude and direction of the Δv imparted by the thrusters, and the range to the RSO. The ΔV can be measured with accelerometers, leaving the range as the free variable to be solved for.

This research will leverage a six Degree-Of-Freedom (DOF) simulation for analysis, but no range measurement will be available. Thus, the viability of a true, angles-only navigation approach for rendezvous operations will be examined in detail. Extensive documentation of the methods, simulations, and results of this analysis were presented at the at the AIAA GNC Conference in Honolulu, Hawaii 2009 [5], and in a Master's Thesis, "Analysis of Square-Root Kalman Filters for Angles-Only Orbital Navigation and the Effects of Sensor Accuracy on State Observability", by J. Schmidt [6].

2.5 Procedure for Determining Collision Probability During Proximity

Most of the current literature on orbital collision probability estimation assumes that the two space objects of interest are in close proximity for only a brief period of time and that there is a high relative velocity between them. It follows that most current methods assume the relative motion to be rectilinear and that the position and velocity error covariance do not change during the encounter. These approximations are valid for the majority of orbital scenarios, but are not valid during orbital proximity operations, e.g. during satellite inspection. This warranted the development of a new procedure to deal with the case in which the encounter occurs at low relative velocities, over longer periods of time, and for which the relative trajectory is not confined to rectilinear motion.

The algorithm that was developed utilizes a series of metrics that can be placed into two main categories. The first category provides an estimate of the instantaneous collision probability. This also places an upper bound on this probability. The second category of metrics provides an estimate of total collision probability. The metrics are arranged in a hierarchy such that those metrics which can be computed quickly are calculated first. As the algorithm progresses the metrics become more costly to compute, but yield more accurate estimates of collision probability. Each metric is compared to a threshold value. If it exceeds the limits determined by mission constraints the algorithm seeks a more accurate estimate by calculating the next metric in the series. If the limit is not reached it is assumed there is a tolerable collision risk, and the algorithm is terminated. In this way the algorithm is capable of adapting so that it is sufficiently

accurate without needless calculations being performed. This approach provides a conceptual framework in which collision probability can be systematically estimated.

Although not complete, the procedure developed thus far has real potential for onboard real-time applications, i.e. it simple and fast. It is based on a variety of metrics including a pseudo- Monte Carlo method in which relative orbital elements are used to drastically reduce the number of required. The proposed procedure will be presented at the AAS/AIAA Space Flight Mechanics Meeting in New Orleans, Feb, 2011.

3   METHODS, ASSUMPTIONS, AND PROCEDURES

3.1   Basic Mission Planning for LEO/GEO Space Operations

In this analysis, the environment parameters are sun angles, range-to-RSO, and relative orientation. The analysis is focused on algorithms that can control sun-angle, relative position, orientation, and zoom to obtain a desired resolution and lighting condition. The sun-angle is initially set such that the sun is directly behind the inspector as it images the object of interest. The orientation of the inspector is constrained to point at the object with an arbitrary roll angle about the camera bore sight.

It is also assumed that the mission planner will be required to autonomously plan the activities of the spacecraft 2-3 orbits ahead. The analysis here focuses on two components of mission and trajectory planning: 1) calculating the Δv required to station-keep at a desired sun-angle and distance from the object, i.e. the Δv required for inertial station-keeping, and 2) the calculation of optimal maneuvers for proximity operations. These calculations are achieved using the Clohessy-Wiltshire (CW) equations in a Local-Vertical, Local-Horizontal frame (LVLH) located at the center of mass of the RSO vehicle. The components of the relative position R^{lvlh} are altitude, downrange, and cross-track. The CW equations are only valid when the RSOs are in near-circular orbits and relatively close to one another. Using these equations, semi-analytically approaches are used to compute constant-lighting, station-keeping Δv and optimal maneuvers to desired lighting conditions.

3.2.   Optimal Inspection of Satellites Ensuring Lighting and Views of All Sides

At each sample time, it must be decided which RSO should be characterized by each Observer. To represent these decisions, let $U \in R^{n \times m \times N}$ be a control tensor where n=the number of Resident Space Objects (RSO's), m=the number of observers, and N=the number of sample times. Each Observer separately samples RSOs at every sample time. Each entry of U is a real variable on [0, 1] such that u_{ijk} indicates the percentage of sample time k that RSO i will be sensed by Observer j. Due to a number of factors including the distance, lighting, etc., the observations will have different levels of quality. Let $Q \in R_+^{n \times m \times N \times M}$ denote a quality of observation tensor found off-line from the physics and orbital simulations, where q_{ijkl} denotes the quality of observing RSO i from Observer j during sample k on the lth side. Note that $q_{ijkl} \geq 0$. If $q_{ijkl} = 0$, then that viewpoint is of zero quality. Larger q_{ijkl} implies that a higher quality measurement is available. Calculation of Q will be explained in Section 3.1.1. This study has found a convex formulation for calculating the sensing plan, U, which provides high quality, Q. Full details are available in [2].

7

3.2.1 Calculating the Quality Tensor, Q.

The quality of observation can depend upon many factors, such as the distance between the RSO and Observer, lighting, the ability to transmit the gathered data, etc. Once images are collected, several techniques are available for automatically determining their quality ([7], [8], [9], and [10]). However, these methods presume an image has already been obtained. Furthermore, although they have been used extensively on images taken by space platforms of terrestrial objects, they have not been used much on images of space objects taken by space objects. This study, in contrast, develops methods for estimating the potential quality of the measurement before an image has been obtained. It models calculation of quality when satellite to satellite images are occluded, have poor lighting angles, are on the dark side of Earth, or are blurred due to diffraction. This grant motivated the inclusion of lighting and multiple sides in particular, so these models will now be presented in more detail. More information can be found in [2].

3.2.2 Incorporating Diffraction, Line-of-Sight, and the Lighting Angle.

The quality factor due to diffraction induced blurring is inversely proportional to the distance between the RSO and the Observer. Using the Rayleigh criteria, this leads to the following formula:

$$q_{blur_{ijk}} = d/(1.22\lambda\delta_{ijk}) \qquad (1)$$

where $q_{blur_{ijk}}$ is the quality factor due to blurring, d is the aperture of the camera, λ is the wavelength of light and δ_{ijk} is the distance between RSO i and Observer j at time k.

When simulating the orbits to calculate δ_{ijk}, it is also verified that there is a clear line of sight between the RSO and the Observer, i.e. that the RSO is not occluded by the Earth from the Observer's vantage point. If it is occluded, then $q_{los_{ijk}} = 0$; otherwise $q_{los_{ijk}} = 1$. Similarly, it is easy to determine *a priori* if the RSO is in the sunlight at any given sample time. If RSO i is in the sunlight at sample k, then $q_{sun_{ijk}} = 1$ for all j. Otherwise, $q_{sun_{ijk}} << 1$ for all Observers j. This incorporates into the model the concept that dark images are of much lower quality than illuminated images.

When imaging satellites, the angle of the light with respect to the viewing axis is extremely critical due to the combination of a single dominant light source (the Sun) and highly reflective surfaces on man-made RSOs. The situation can be likened to viewing a highly textured, shiny object illuminated by a single spotlight in a darkened theater. Let $v_{RO_{ijk}}$ denote the unit vector from Observer j to RSO i during sample k, and let v_{ES} be the unit vector from the Sun to Earth (see Figure 3). Then

$$\alpha_{ijk} = \arccos(v_{RO_{ijk}}^T v_{ES}) \qquad (2)$$

is the angle between the viewing axis and incoming sunlight. Due to the highly reflective surfaces on man-made RSOs, the image contains much specular glare when α_{ijk} is near 0. On the other hand, if $|\alpha_{ijk}| > 90^o$, RSO i is back-lit by the Sun. This can produce a sharp silhouette, but otherwise has less detail. A good compromise might be $|\alpha_{ijk}| \approx 45^o$.

Like the other factors, the lighting angle quality factor (q_{lit}), modulates overall quality, so it is desirable to let it take on values from the interval [0, 1]. One suitable function is

$$q_{lit} = \begin{cases} q_{lit,min} + (1 - q_{lit,min})\sin^2 2\alpha, & |\alpha| \leq 90^o \\ \qquad q_{lit,min}, & |\alpha| \geq 90^o \end{cases} \qquad (3)$$

where $q_{lit,min} \in$ [0, 1] specifies the quality (usually near zero) of back-lit and head-on images. This function is illustrated in a polar plot for $q_{lit,min} = 0.2$ in Figure 3. Note that this function is not unique. Other functions can be developed to precisely model the exact conditions of a specific application. A look-up table can be utilized to represent $q_{lit}(\alpha)$, if necessary. Also note that the lighting issues are very different for ground based observers viewing RSOs. In this case, the optimal viewing may be just before the Sun rises, or just after it sets. At these times, a ground based telescope is in the dark and therefore has less ambient noise, but the RSO is still illuminated. Ground based Observers can be incorporated, but this will not be addressed in detail here, where the focus is on orbiting Observers.
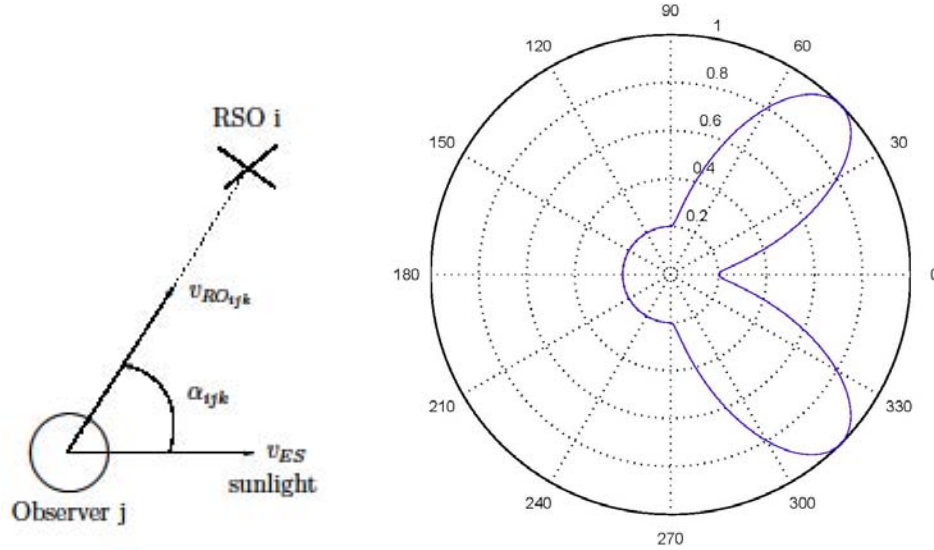
Figure 3. Graphical Depiction of Lighting Angle and Polar plot of qlit(α). Head-on ($\alpha \approx 0$) and Back-Lit ($|\alpha| < 90^o$) Has Low Quality; $|\alpha| \approx 45^o$ Has Highest Quality

3.2.3 Determining the Quality of Viewing All Desired Sides of an RSO.
It is often desirable to image an object along several of its faces. For each RSO, assign outward facing unit normals along each face of interest, i.e. let n_{jl} be the outward facing unit normal on RSO j along the face l. To determine if an Observer can view a given face, let $v_{OR_{ijk}} = v_{RO_{ijk}}$ be the unit vector pointing from RSO j to Observer I at sample k. Then

$$v_{P_{ijk}} = \arg \max_{l=1,\cdots n_{v_i}} (n_{jl}^T v_{OR_{ijk}}) \qquad (4)$$

9

denotes the viewpoint number for observation ijk, since this function returns the maximizing argument (viewpoint number), not the maximum dot product. The fourth subscript on quality incorporates the viewpoint number, while n_{vi} denotes the number of viewpoints to be observed on RSO i. This is then used to set the quality of observation along all faces that are not currently in view to zero as follows:

$$q_{view_{ijkw}} = \begin{cases} 1, & v_{p_{ijk}} = w \\ 0, & otherwise \end{cases} \tag{5}$$

3.2.4 COMBINATION INTO A SINGLE QUALITY METRIC.

In order to form a single number that reflects overall quality of RSO i's measurement by Observer j during sample k along face l, q_{ijkl}, let

$$q_{ijkl} = q_{blur_{ijk}} * q_{los_{ijk}} * q_{sun_{ijk}} * q_{lit}(\alpha_{ijk}) * q_{view_{ijkl}} \tag{6}$$

For the usual (long) distances between satellites, quality is primarily determined by diffraction induced blurring ($q_{blur_{ijk}}$). The remaining quality factors are in the interval [0, 1], and modulate the baseline quality to ensure an unobstructed view that is well lit from good viewing angles on a given face (l). This quality model is then included into our new algorithm for calculating the sensing plan, thereby obtaining quality images.

3.3 Homography-Based Change Detection

Now that methods for obtaining high quality images have been developed, the images can be analyzed to determine if changes have occurred in the RSOs. Two methods (homography and pose based) have been derived.

The homography-based change detector takes two inspection images of an RSO and identifies areas of the RSO where its visible appearance is not the same in both images. The first image, or base image, is denoted I_1 and is taken from the camera coordinate system $\{o_1\}$. The second image, or comparison image, is taken from a different location after a period of time has elapsed. The comparison image is denoted I_2 and is taken from system $\{o_2\}$. The combination of position and orientation between the camera and RSO is called the pose of a given scene. Since images I_1 and I_2 contain different poses, it is not possible to compare the images without adjusting for these differences.

Satellites frequently contain highly planar surfaces, such as solar arrays. In addition, the distance between the camera and the RSO is much larger than the distances in the relief of the RSO. Therefore, it is possible to simplify the multiple view geometry of the image by assuming that all of the visible points on a RSO lay in a single plane. This permits the use of a planar homography approach. The homography based change detector generates a homography, H, between I_1 and I_2. If two corresponding normalized image points x_1 and x_2 can be found in images one and two, respectively, then

$$x_2 * Hx_1 = 0 \qquad\qquad (7)$$

where * denotes the cross product here. By writing the above equation for every pair of matched points, H can be found using the least squares method. The linear mapping described by H is used to warp I_1 so that it appears as though it was taken from $\{o_2\}$. Image subtraction and thresholding are used to perform change detection. Finally, a morphological filter is used to smooth out the homography estimation error. More details are available in [3].

3.4   Pose-Based Change Detection

The pose (combined position, T, and rotation matrix, R) can be used to compare two images with large differences in viewpoint, as long as a model of the RSO is known. This pose-based change detector takes two images of an RSO, I_1 and I_2, and estimates the pose between the two images, R_{21} and T_{12}. New optimal and minimum-eigenvalue 3D algorithms have been developed to perform this pose estimation in the robust manner required of space applications. They are summarized in the Figures 4 and 5 below. Assuming that the pose between the RSO and the base image is known, the pose between the base image and the comparison image can be transformed into the pose between the RSO and the comparison image.

Algorithm 1 Optimal estimation of pose by minimizing weighted 3D error

Given a set of n image correspondence points x_1^i, x_2^i, for $i = 1, 2, \ldots, n$, and $n \geq 5$, this algorithm estimates the pose R, T between the camera coordinate systems, such that the 3D coordinates are related by $X_2^i = RX_1^i + T$. The algorithm minimizes the sum of the 3D errors which have been weighted by a factor inversely proportional to the distance between X^i and the camera.

1. Define the vectors u_j^i which point in the direction of the preimage of correspondence point i in image j. Let $u^i = \hat{u}_2^i R u_1^i$, where $\hat{\cdot}$ denotes the cross product matrix.

2. Define the 3D weighted error $\|e_w^i\|^2 = \dfrac{T^T u^i (u^i)^T T}{\|\hat{u}_2^i T\|^2 + \|\hat{u}_1^i R^T T\|^2}$

3. Define the cost function $J' = \sum_{i=1}^{n} \|e_w^i\|^2$

4. Minimize J' with respect to R and T, subject to $R \in SO(3)$ and $T \in S^2$, using a numerical search.

Figure 4. Algorithm 1 – Optimal Estimation of Pose by Minimizing Weighted 3D Error

11

Algorithm 2 Approximate estimation of pose by minimizing a minimum eigenvalue

Given a set of n image correspondence points x_1^i, x_2^i, for $i = 1, 2, \ldots, n$, and $n \geq 5$, this algorithm estimates the pose R, T between the camera coordinate systems, such that the 3D coordinates are related by $X_2^i = RX_1^i + T$. The algorithm minimizes the sum of the 3D errors which have been weighted by a factor inversely proportional to the distance between X^i and the camera, assuming that the field of view of the camera is sufficiently narrow.

1. Define the vectors u_j^i which point in the direction of the preimage of correspondence point i in image j. Let $u^i = \hat{u}_2^i R u_1^i$, where $\hat{\cdot}$ denotes the cross product matrix.

2. Define $M_s(R) = \sum_{i-1}^n u^i (u^i)^T$

3. Find the rotation matrix R which minimizes the minimum eigenvalue of $M_s(R)$ by performing a numerical search over a sphere of radius 2π.

4. T is the minimum eigenvector of $M_s(R)$, subject to $\|T\| = 1$.

Figure 5. Algorithm 2-Approximate Estimation of Pose by Minimizing a Eigenvalue

It is assumed that a detailed 3D model of the RSO already exists, such as the Computer Aided Design (CAD) model used during its design, or a model generated from many images of the RSO. Using pose estimates from our new algorithms, it is possible to generate I_3, a synthetic image which has the same pose as I_2. Finally, subtraction, thresholding, and morphological image processing are used to perform the comparison between I_2 and I_3. More details are available in [4].

3.5 Angles-Only Navigation for Orbital Proximity Operations

The angles-only navigation analysis was conducted on a high-fidelity 6-dof simulation with an embedded 21 state extended Kalman filter estimator. The performance metrics for this study include navigation errors, trajectory dispersions, and Δv requirements, when applicable. Navigation errors of interest are the true relative navigation position errors and the associated relative navigation position error covariance. Particular attention will be given to the relative range error and variance in order to better understand when and under what conditions the relative range is observable. A brief overview of the simulation and the estimator is provided below. Details are provided in References [5] and [6].

3.5.1 SIMULATION.

The high fidelity, six degree-of-freedom simulation consists of two spacecraft, an inspector and an RSO in low-Earth orbit. The simulation includes sensor, actuator, and dynamic models that include noise, bias, and other errors. Candidate attitude and translational controllers were built for the inspector spacecraft. A quick overview of the satellite simulation may be seen in Figure

6. The main elements are A) dynamics and environment models, B) actuator models, C) sensor models, and an expanded view of the flight computer algorithms D) extended Kalman filter, E) mission manager, and F) attitude and translational control laws.
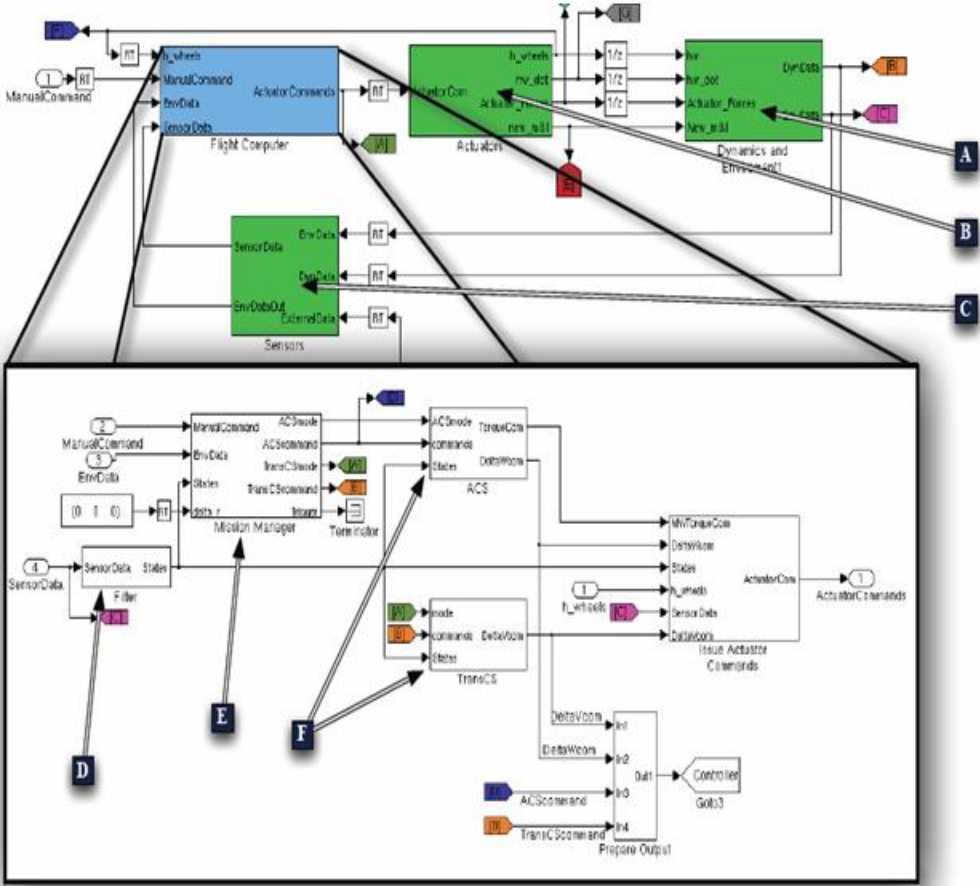
Figure 6. Simulation Overview

The translational dynamics models in the simulation included gravitation acceleration and thruster acceleration. The total acceleration is integrated to obtain inertial position and velocity for both the inspector and the RSO. Euler's equation and quaternion kinematics are used to propagate the inspector and RSO attitude and attitude rate. The torque acting on the inspector is based on thruster firings and momentum wheels. Atmospheric drag and solar pressure models are not implemented in this simulation. However, random accelerations and torques (process noise) are included in both vehicle models to represent to unmodeled accelerations and torques due to drag, uncoupled thruster forces, solar radiation pressure, and self plume impingement. These models were deemed adequate for the investigations conducted here.

The onboard sensors include three-axis accelerometers, a line-of-sight camera for observing the RSO, and a star-camera for determining attitude. The specifications for the accelerometers and LOS camera are found in Figure 7. The accelerometer and Line Of Sight (LOS) camera specifications are categorized as good, average and poor while the star-tracker was assumed to

give perfect measurements. Since the mechanization of the navigation algorithms are in the inertial frame, and since both the star-tracker and the camera are mounted on the same platform (i.e. the inspector), the camera errors effectively represent the sum of star-tracker and camera errors.   The accelerometers provide a measurement of all non-gravitational forces corrupted by misalignment, noise, bias, and quantization effects. The actual values for misalignment and noise are dependent on the specific run. The line-of-sight camera provided the tangent of the azimuth and elevation angles corrupted by misalignment and noise. The actual values for misalignment and noise are also dependent on the specific run. For this simulation, a perfect star-camera was used to define orientation of the body frame. The effect of any non-zero star-camera errors was easily modeled as LOS-camera error and accelerometer misalignment.

Accelerometers			
	Noise Strength 1σ per axis	Bias 1σ per axis	Misalignment 1σ per axis
good	$3 \times 10^{-9} m^2/s^3$	$3 \times 10^{-4} m/s^2$	$1 \times 10^{-5} rad$
average	$3 \times 10^{-7} m^2/s^3$	$3 \times 10^{-3} m/s^2$	$1 \times 10^{-4} rad$
poor	$3 \times 10^{-5} m^2/s^3$	$3 \times 10^{-2} m/s^2$	$1 \times 10^{-3} rad$
The nominal accelerometer performance is good			
Accelerometer quantization is held fixed at $1 \times 10^{-9} m/s^2$			

Line-of-Sight Camera		
	Measurement Noise 1σ per axis	Misalignment 1σ per axis
good	$1 \times 10^{-5} rad$	$1 \times 10^{-5} rad$
average	$1 \times 10^{-4} rad$	$1 \times 10^{-4} rad$
poor	$1 \times 10^{-3} rad$	$1 \times 10^{-3} rad$
The nominal LOS camera performance is good with misalignment 1σ set to $1 \times 10^{-6} rad$		

Figure 7. Accelerometer and Line-of-Sight Camera Specifications

Actuators for the inspector satellite include 12 thrusters for translation and attitude control, and four momentum wheels for more precise attitude control. The 12 thrusters on the inspector satellite are located a half meter from the center of mass. The nominal force of each thruster is 0.1 N.   Other thruster specifications are shown in Figure 8. Note that the thrusters are in pairs and can be used to generate force and torque. The thrusters are either on or off. The moment wheel system is actually four wheels that work together to generate torques around the three primary axes.

Thruster Force model Specification		
Spec	Value	Units
Noise Strength	1×10^{-8}	$(N\,s)^2/_s$
Bias Variance	1×10^{-8}	$(N)^2$
Bias Time Constant	60	sec
Misalignment Standard Deviation	20 arcseconds	rad
Scale factor	100×10^{-6}	PPM

(a) Thruster Force Model Specifications

Thruster Torque model Specification		
Spec	Value	Units
Noise Strength	1×10^{-6}	$(N\,m\,s)^2/_s$
Bias Variance	1×10^{-6}	$(N\,m)^2$
Bias Time Constant	60	sec
Misalignment Standard Deviation	20 arcseconds	rad
Scale factor	100×10^{-6}	PPM

(b) Thruster Torque Model Specifications

**Figure 8. Thruster Specifications – (a) Force Model, (b) Torque Model**

Translational control was achieved via a station-keeping Proportional-Derivative (PD) control law. Attitude control achieved with two attitude controllers: a phase-plane controller for the thrusters, and a Proportional-Integral-Derivative (PID) controller for the momentum wheels. When the errors are large, the thrusters are used to correct attitude by way of a phase-plane controller. When the errors are small enough to be handled by the momentum wheels, the phase-plane controller is deactivated and a PID controller uses the momentum wheels for precision pointing. Details and gain selection for all three control laws can be found in References [5] and [6].

Translational guidance consisted of a simple station-keeping/position tracking command. The inspector is commanded to hold or track a desired position in the LVLH frame. The attitude guidance consisted of a simple RSO tracking command. The command issued by the algorithm would orient the inspector such that the LOS camera would point at the RSO.

3.5.2 Extended Kalman Filter.
The extended Kalman filter is a 21 state filter that updated the state and state covariance when angle measurements are available, and propagates the state and state covariance matrix in between measurements using dynamical models and accelerometer data. The filter state consists of the inertial position and velocity of the inspector and the RSO (12 states), as well as accelerometer misalignment (3 states) and bias (3 states), and line-of-sight camera bias (3 states). Note that the gyro data is only used to propagate the attitude in between star-camera

measurements. Detailed equations and gain selection for the filter can be found in References [5] and [6]. A high-level overview of the filter given in Figure 9 shows the important components of the filter including A) measurement and measurement partial derivative calculation, B) quaternion to direction-cosine-matrix calculation, C) state propagation, D) state transition matrix calculation, E) exponential decay to smoothly incorporate accurate angle measurements, F) state and state covariance update calculations, G) process noise mapping matrix calculation, and H) state covariance propagation.
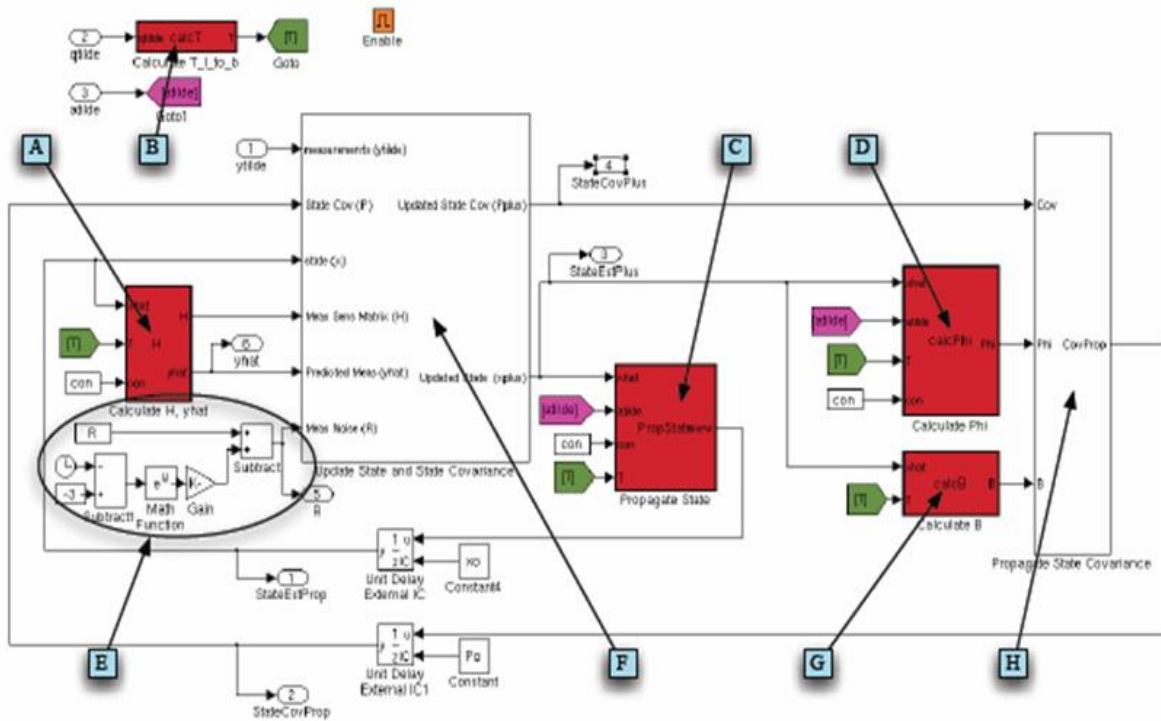
Figure 9. Extended Kalman Filter Implementation

3.6   Procedure for Determining Collision Probability during Proximity

The Clohessy-Wiltshire (CW) or Hill's equations are used to model the dynamics of the relative position and velocity as well as the dynamics of the relative position and velocity covariance matrix. It is assumed that the inspector vehicle is in an orbit that is only slightly displaced from that of the RSO in a near circular orbit. The reference frame for the CW equations is centered at the RSO with the x-axis pointing up or opposite the gravity vector, the y-axis is in the direction of the local horizontal or roughly aligned with the target velocity vector, and the z-axis is normal the orbit plane.

With these relatively simple assumptions, mathematical expressions and algorithms for several instantaneous probability-of-collision metrics and several total probability-of-collision metrics were developed and can be found in [11]. The instantaneous probability-of-collision metrics are handled with either a fast analytical approach for calculating the horizontal and vertical ellipsoidal projections of the covariance matrix, or a more Central Processing Unit (CPU) intensive approach for calculating the ellipsoid projection and the Mahalanobis distance. The

16

total probability-of-collision metrics are handled by a method developed by Patera [12] and by a fast pseudo-Monte Carlo method that was specially designed for this research.

The instantaneous horizontal and vertical metrics are computed analytically and are given by the minimum value of d_h, the ratio of the inspector-RSO horizontal separation (y) to the relative horizontal uncertainty (σ_h), and the minimum value of d_v, the ratio of the inspector-RSO vertical separation (x) to the relative vertical uncertainty (σ_v), over the desired time period of interest, where

$$d_h = \frac{y}{\sigma_h} = \frac{y}{\sqrt{i_h^T P_{rr} i_h}} \tag{8}$$

$$d_v = \frac{x}{\sigma_v} = \frac{x}{\sqrt{i_v^T P_{rr} i_v}} \tag{9}$$

and where P_{rr} is the covariance of the relative position, i_v is the unit vector in the direction of the local-vertical, and i_h is a unit vector in the direction of the local-horizontal. If these simple metrics are less than a pre-selected threshold, the risk of a collision is acceptable and the algorithm is terminated. If either of the metrics is above the threshold, the algorithm goes on to calculate a more accurate metric for the collision probability.

The calculation of the total projection metric is more CPU intensive and is given by the minimum value of d_p, the ratio of the inspector-RSO range (|r|) to the relative range uncertainty (σ_r), over the desired time period of interest, where

$$d_p = \frac{|r|}{\sigma_r} \frac{|r|}{\sqrt{i_r^T P_{rr} i_r}} \tag{10}$$

If this metric is less than a pre-selected threshold, the risk of a collision is acceptable and the algorithm is terminated. Otherwise, the algorithm goes on to calculate a more accurate metric.

The final and most accurate metric of the instantaneous probability-of collision is the Mahalnobis distance and is given by minimum value of d_m over the desired time period of interest, where

$$d_m = |r|\sqrt{i_r^T P_{rr}^{-1} i_r} \tag{11}$$

This last instantaneous metric is slightly more CPU intensive since is requires the repeated evaluation of the inverse of a 3x3 matrix. If this metric is less than a pre-selected threshold, the risk of a collision is acceptable and the algorithm is terminated. Otherwise, the algorithm goes on to calculate more reliable metrics for the *total* probability-of-collision.

The first total probability calculation is based on an approach developed by Patera [11]. This technique is relative simple and fast, however, tests have shown that this algorithm is not always

17

accurate or reliable, especially when the relative velocities are low.   Thus, the total probability calculated by this algorithm is multiplied by a fact of twenty for conservatism. If this metric is less than a pre-selected threshold, the risk of a collision is acceptable and the algorithm is terminated.   Otherwise, the algorithm goes on to calculate a yet more reliable metric for the total probability-of-collision.

The final algorithm is a pseudo-Monte Carlo algorithm. This is a fast Monte Carlo approach that eliminates most of the samples simply by examining the relative orbital elements of each sample, thereby quickly determining whether or not a collision is even possible. If not, the sample is rejected. If a collision is deemed possible, the distance of closest approach is determined and compared to the minimum distance for a collision. In this way, a reliable and accurate calculation of the total probability-of-collision is computed, albeit as the expense of some significant but reasonable CPU time. More details can be found in [11]

4   RESULTS AND DISCUSSION

### 4.1   Basic Mission Planning for LEO/GEO Space Operations

As an inspection spacecraft maintains constant range and sun angles relative to a space object, i.e. inertial station-keeping, the relative motion in the LVLH frame traces out a circle as shown in Figure 10. This relative motion trajectory is generated by rotating the relative position vector of the inspector about the orbit normal at the orbital frequency (in the opposite direction).
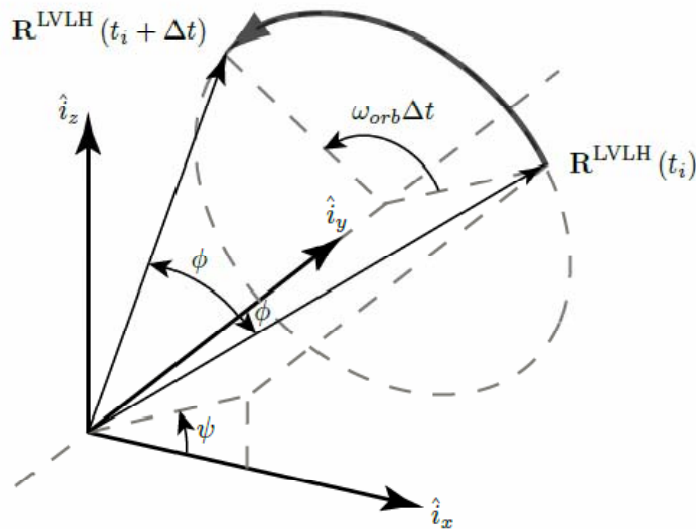

Figure 10. Geometry of Station-Keeping with Constant Lighting Conditions

The Δv required for station-keeping under continuous thrust for a time Δt can now be found using the CW equations which provides an expression for the specific force required to maintain constant range and constant sun-angles relative to the space object, i.e. to maintain a constant inertial position relative to the space object. The integration of this expression results in the Δv

required for inertial station-keeping. An example is shown in Figure 11. In an effort to generalize the results, three cases are considered over the course of two orbital periods. For each case the sun-angle φ is varied from 0 to 90 degrees in 10 degree increments. The results can further generalized by noting that the Δv can be obtained by analytically integrating the specific force in the CW equations to obtain $\Delta v = R/P * K(\varphi,n)$ where R is the range to the RSO, P is the orbital period, n is the station-keeping duration in terms of number of orbits, and the function $K(\varphi,n)$ is plotted Figure 12.
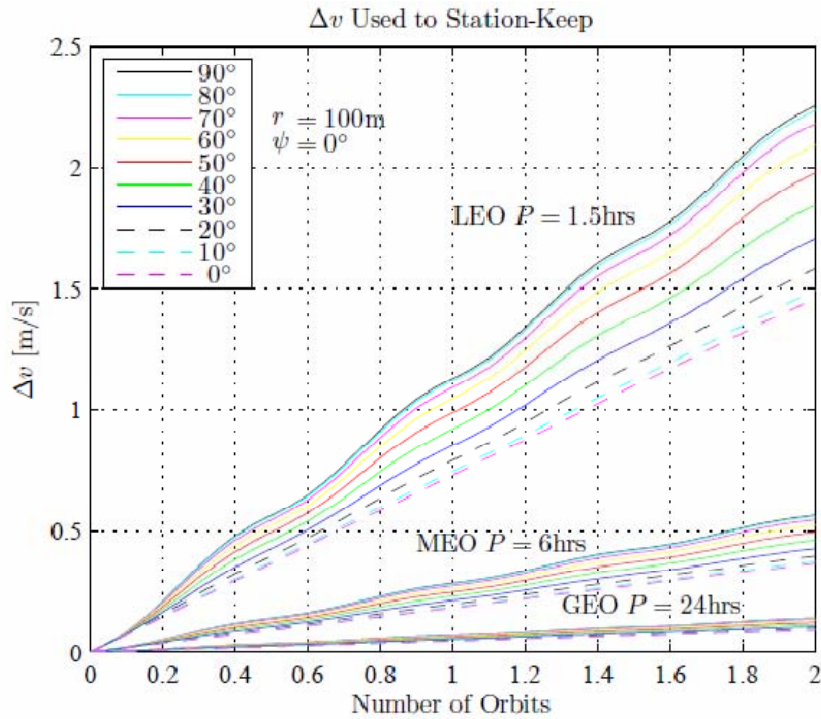

Figure 11. Examples of Δv Used for Station-Keeping as a Function of Time, Sun-Angle, and Orbit (LEO, MEO, and GEO)
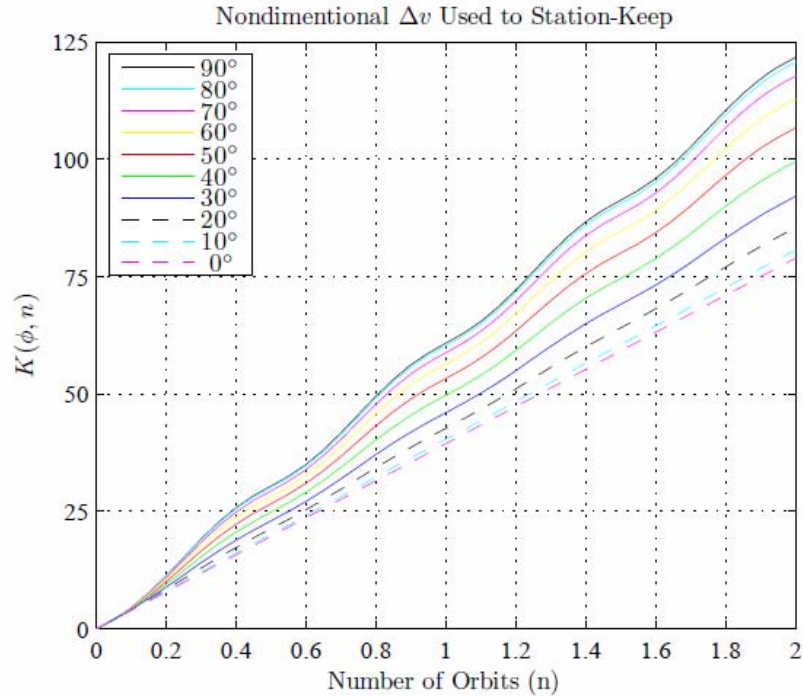
Figure 12. Examples of the Δv Used for Station-Keeping as a Function of Number of Orbits

It is also important to minimize the propellant used during proximity operations. If constant lighting conditions are achieved by using inertial station-keeping, the CW equations can be used to determine an optimal transfer time from the current range and lighting conditions to any new range and lighting condition. Since it assumed that inspector will be station-keeping before the transfer, its initial velocity will be a known function of time as described by Figure 10. Additionally, it is assumed that the inspector will be required to station-keep after the transfer, so its final position and velocity will also be known as a function of time. By using this information, the CW equations can be used to derive an analytical expression for the total maneuver Δv as a function of time [1]. The optimal transfer time is determined by finding the time that minimizes this total maneuver Δv. A sample case is show in Figure 13 below. These types of optimization problems are not difficult to solve and can easily be added to an onboard GN&C system. This includes cases or scenarios where maneuver times may be constrained by other operational considerations.
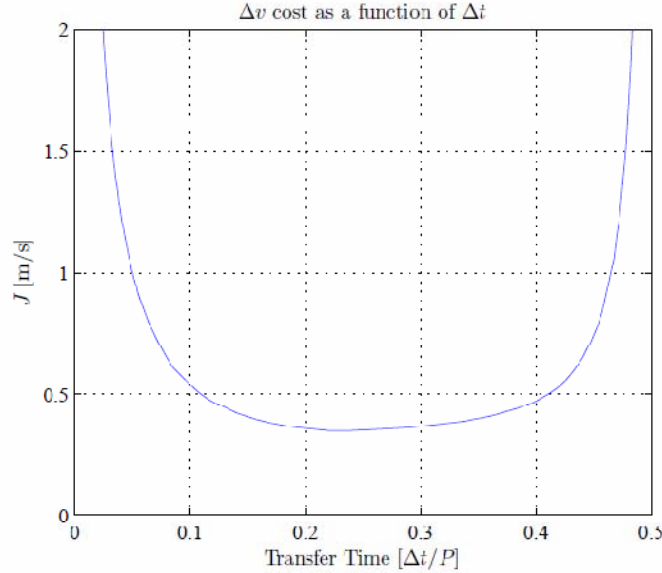
Figure 13. Example of Transfer From a Sun Angle of 20° and a Range of 175m to a Sun Angle of 45° and a Range of 50m in LEO

4.2   Optimal Inspection of Satellites Ensuring Lighting and Views of All Sides

To solve the optimizations, the freely available software "cvx" has been employed. Although the theory is completely general for 3-D orbits, most of the simulations are performed in 2-D to clarify the presentation. In the plots, Observers are indicated by green circles and RSOs by red x's. The width of a line connecting an Observer to an RSO is proportional to the percentage of that sample time during which the Observer collects data from the corresponding RSO, and the size of the RSO is proportional to the total quality of its observation, J_{il}, at the current sample time. All plot units are kilometers.

Figures 14-15 illustrate the use of weighting to emphasize characterization of a key RSO by 100 %. As anticipated, the final total quality of characterization of the emphasized RSO (at approximately 11:00) is almost exactly twice that of the least characterized RSO. The binary approximation (Figure 15) is also very close to optimal.

Figures 16 and 17 illustrate the adjustment of weights to emphasize observation during a given time interval. In this case, one RSO is weighted so that it will be observed during the first half of the simulation. Figure 17 illustrates the results halfway through the simulation–the desired RSO (10:00) is much larger, as it has already been thoroughly characterized. For the second half, that RSO receives little additional attention, since efforts must now be concentrated on the less characterized RSOs. The final results provide approximately equal total observation of all RSOs (Figure 17).

Figure 18 demonstrates the full power of the technique by implementing all of the quality terms. In this case, sunlight is modeled as coming from the left side of the screen, i.e. $v_{ES} = [0 - 1]^{T}$. Note that all RSOs are of nearly equal size at the final time, indicating high quality observations

of all RSOs. This occurs despite the two new constraints (that the RSOs not be in the dark, and that the lighting angle be good). This simulation sets $q_{sun, min} = 0$, so quality goes to zero when an RSO is in the dark. Consequently, even though the Observer at ≈9:00 is very close to three RSOs and has a clear line-of-sight to them, it is not performing any Observations because all of these RSOs are in the dark. The red Observer (at ≈6:00) is slightly closer to its nearest RSO than the green Observer (at ≈3:00). Consequently, $q_{blur, red} = 39.9$, while $q_{blur, green} = 31.0$. However, the lighting angle is much better for the green Observer than the red, whose RSO is back-lit by the Sun from this viewing angle. In fact, $q_{lit,red} = q_{lit,min} = 0.2$, while $q_{lit,green} = 0.74$. The overall quality of observation of the RSO is the product of these factors, hence $q_{red} = 7.97$ vs. $q_{green} = 23.0$.
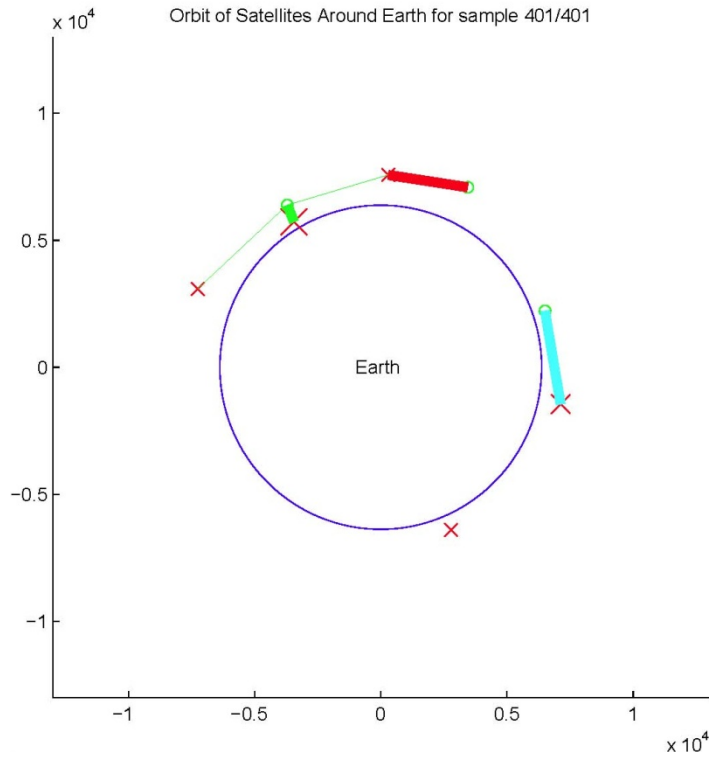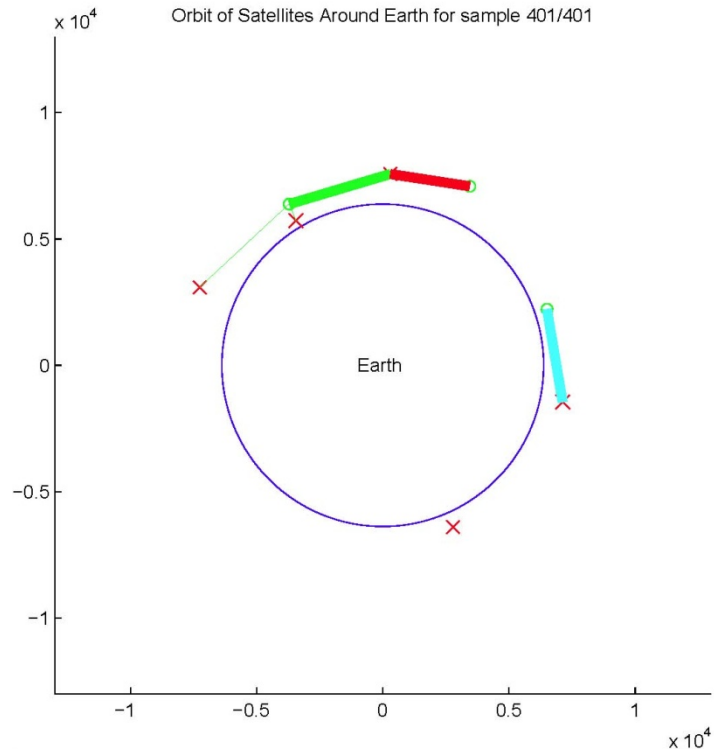

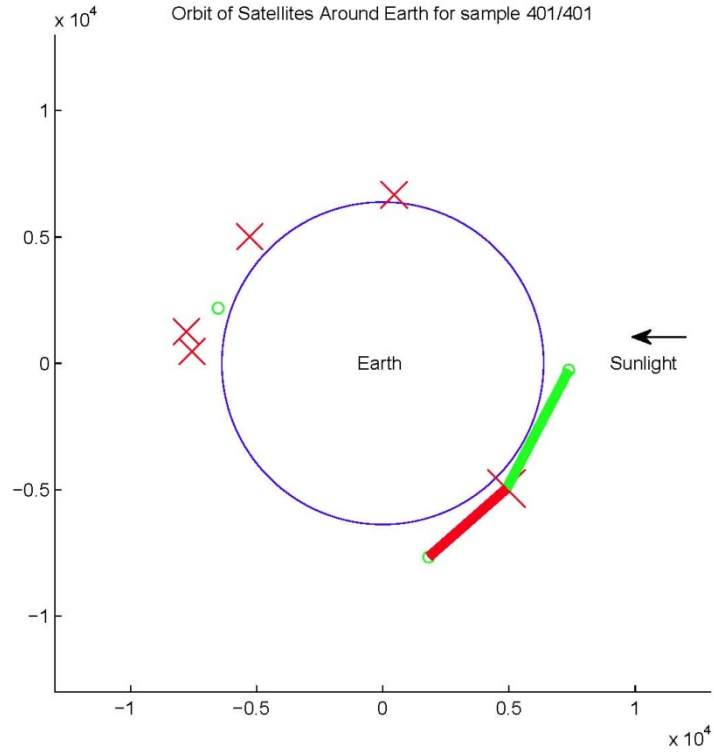**Figure 14. Orbital simulation for the last sample time**
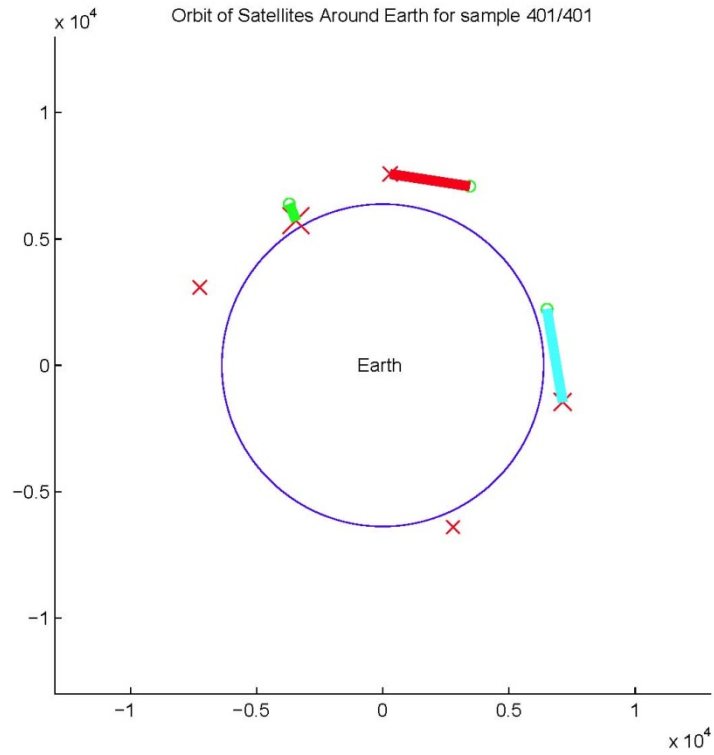
Figure 15. Binary Orbital Simulation Depicted at the Last Sample Time
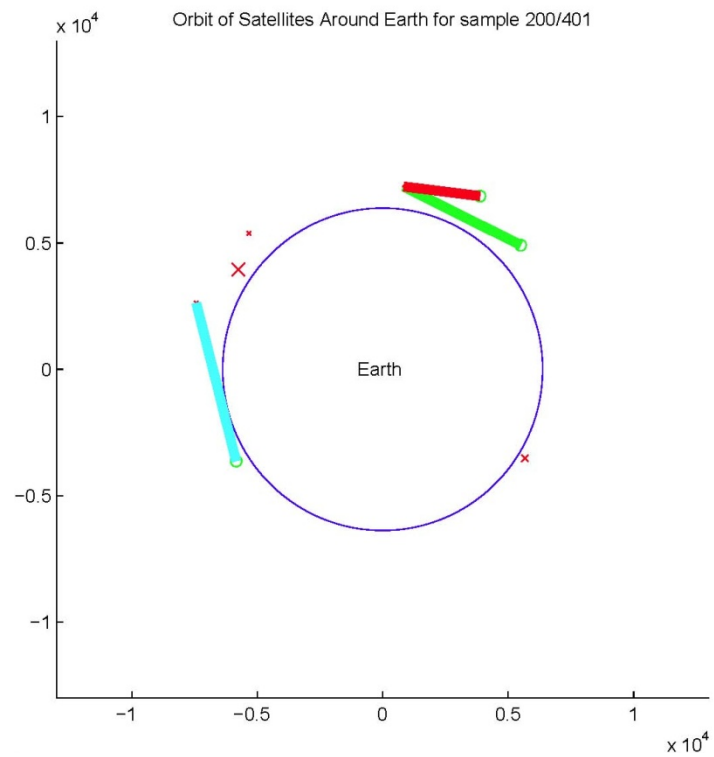
Figure 16. Orbital Simulation for the Middle Sample Time

**Figure 17. Orbital Simulation for the Last Sample Time**

Figure 18. Orbital Simulation for the Last Sample Time

24

4.3 Homography-Based Change Detection

To evaluate the performance of the Homography-Based Change Detection algorithm, it was tested using computer-generated images of satellites in orbit. The majority of the testing was accomplished using a 3D model of the Aura satellite. The Aura spacecraft is made up of a main body covered in gold foil with a single large solar array to the side. This spacecraft was selected for use in these simulations due to its combination of a nearly planar surface (the solar array) and non-planar surfaces (the spacecraft body and antennas). A small, gray box with beveled edges was placed on the spacecraft body to test the algorithm's ability to detect its removal.

To determine the importance of accurate image correspondence points, testing was performed using correspondence points selected by hand and correspondence points generated using the Scale Invariant Feature Transform (SIFT). The images which were used to test the algorithm are presented in Figure 19. Note that each image has a slightly different pose, and that the gray box attached to the upper right corner of the RSO in I_1 has been removed in I_2. This simulates an RSO which has suffered damage in the time that elapsed between the two images.
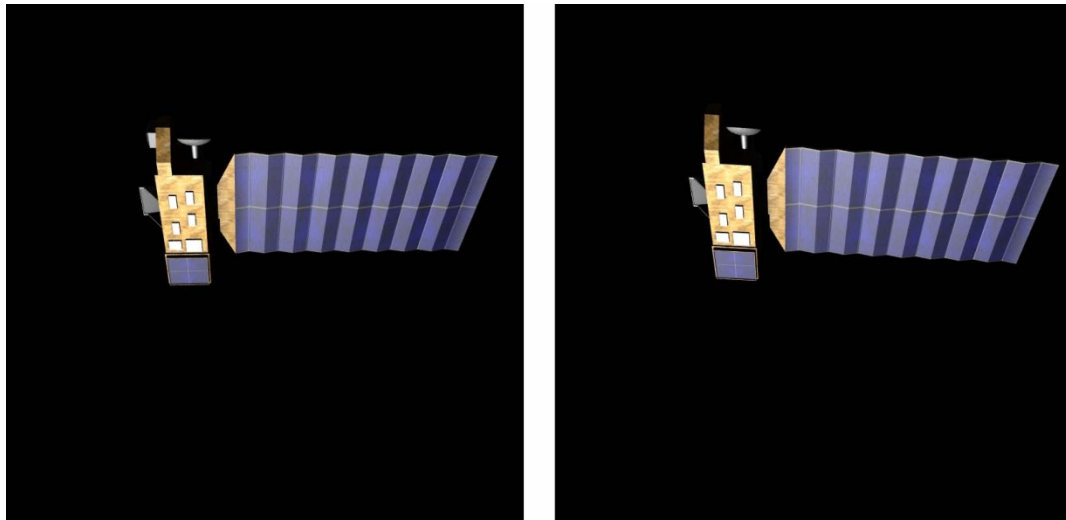
Figure 19. Test Images: (a) Base Inspection Image I_1, (b) Comparison Inspection Image I_2

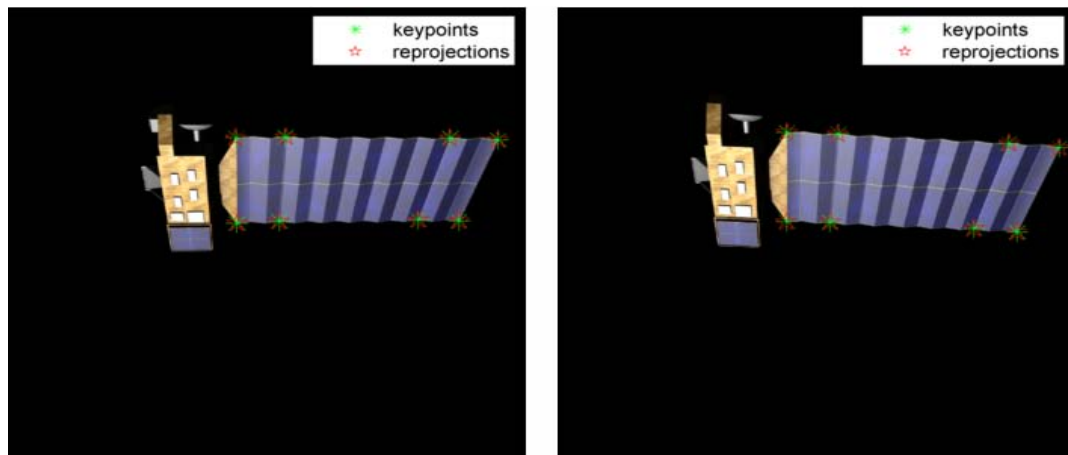#### 4.3.1 Manual Correspondence Points.

To ensure accuracy, the image correspondence points used to estimate the homography between the images are first selected by hand. These correspondence points are shown as green asterisks in Figure 20. The majority of the correspondence points are placed on the solar array, which is nearly planar. This produces the best estimate of the actual homography.

In order to estimate the accuracy of the homography, the image correspondence points are re-projected. These re-projections are denoted by the red stars in Figure20. A good homography estimate will produce re-projections which are close to their measured correspondence points.

The result of warping I_1 to the viewpoint of I_2 is shown in Figure 21. Note that the box is present in this image, since it was present in I_1.

The result of directly subtracting I_1 and I_2 is given in the left part of Figure 22. The change in pose is not taken into account, as no homography estimation or warping is used. As a result, the pose differences between these two images have been identified as changes in regions of the satellite which did not in fact change. This simplified method is not sufficient for cases where even minor changes in pose may occur.

Compare this to the result in the right part of Figure 22 obtained by subtracting the warped version of I_1 and an unmodified version of I_2. Compared to the left image, the right image looks skeletal, as the warped image is much closer to the true image. The thin nature of these errors makes it trivial to find and remove them using morphological filtering. A morphological erosion filter utilizing a ball-shaped structuring element with a radius of five pixels was applied to the right image in Figure 22. This produced an eroded difference image. Finally, the eroded difference image was converted to a binary image using Otsu's method. This produced a blank image except for one white spot where the box was located (Figure 23). Consequently, the homography-based change detection algorithm has successfully flagged the absence of the gray box on the upper right corner of the RSO.
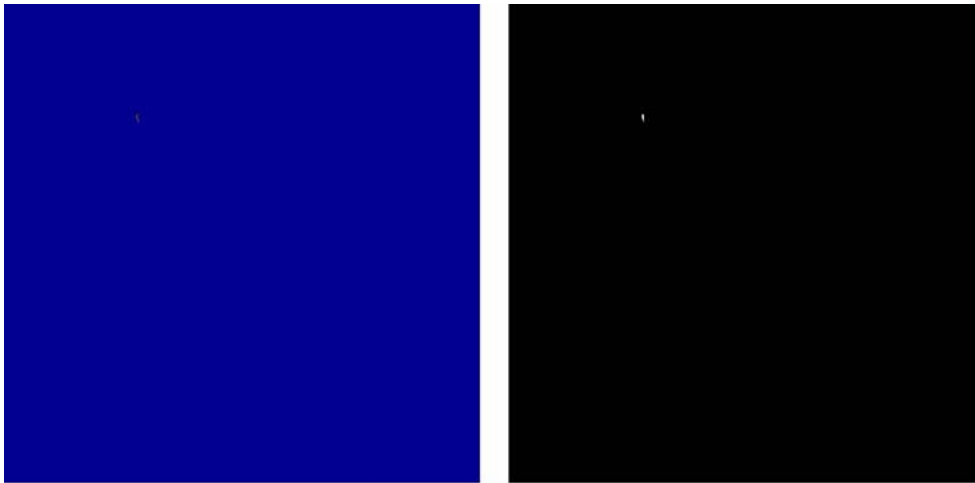

Figure 20. Manual Correspondence Points
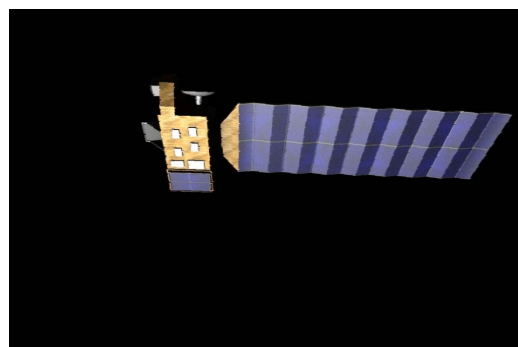
Figure 21. Warped Image

26
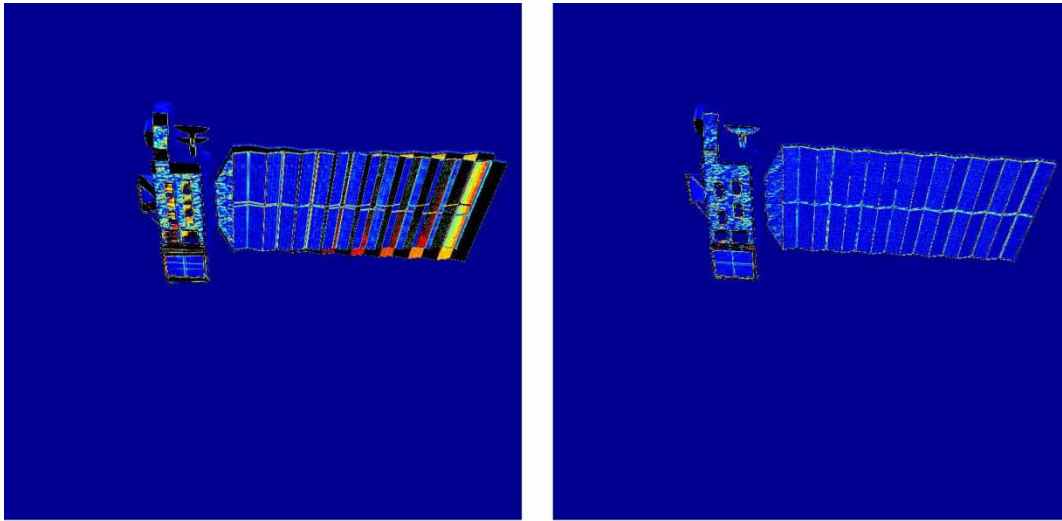
Figure 22. Comparison of Difference Images - (a) Direct Difference of Image I_1-I_2, (b) Warped Difference Image

Figure 23. Removal of Homography Errors

Note: See the above Figure 23 - (a) Eroded warped difference image appears blank due small differences in colors, but, (b) with binary thresholding the change detection result shows one white spot where the box was added to the RSO in the upper left corner. This spot is easy for a machine to detect.

4.3.2 Automatic Correspondence Points.

The same images used in the previous section are processed using automatically generated correspondence points. The correspondence points are selected automatically using the Scale Invariant Feature Transform. For the pair of images in Figure 19, approximately 140 SIFT

features are found in each image. Of these features, 40 are determined to be correspondence points using Lowe's algorithm. These correspondence points are shown in Figure 24.

The correspondence points are used to generate a homography estimate. This homography estimate produces the re-projections given in Figure 25. Note that due to the noise in the correspondence points, and due to the increased number of correspondence points which do not reside on the homography plane, these re-projections are not as accurate as those in Figure 20.

The warped version of I_1 is given in Figure 26. Again, the box is visible in the image.

The difference image between I_2 and the warped image I_w is given in Figure 27(b). For ease of comparison between the manual and automatic results, the difference image generated using manually selected correspondence points from Figure 22(b) has been repeated as Figure 27(a). The manual correspondence points generate a noisy difference image with stronger homography errors.

Due to the increased amount of homography error, a more aggressive morphological filter is needed. A ball-shaped structuring element with a radius of seven pixels is used to generate the eroded difference image in Figure 28(a). Applying Otsu's method and thresholding produces the change detection result in Figure 28(b). Again, the algorithm has detected the loss of the box on the upper corner of the satellite.
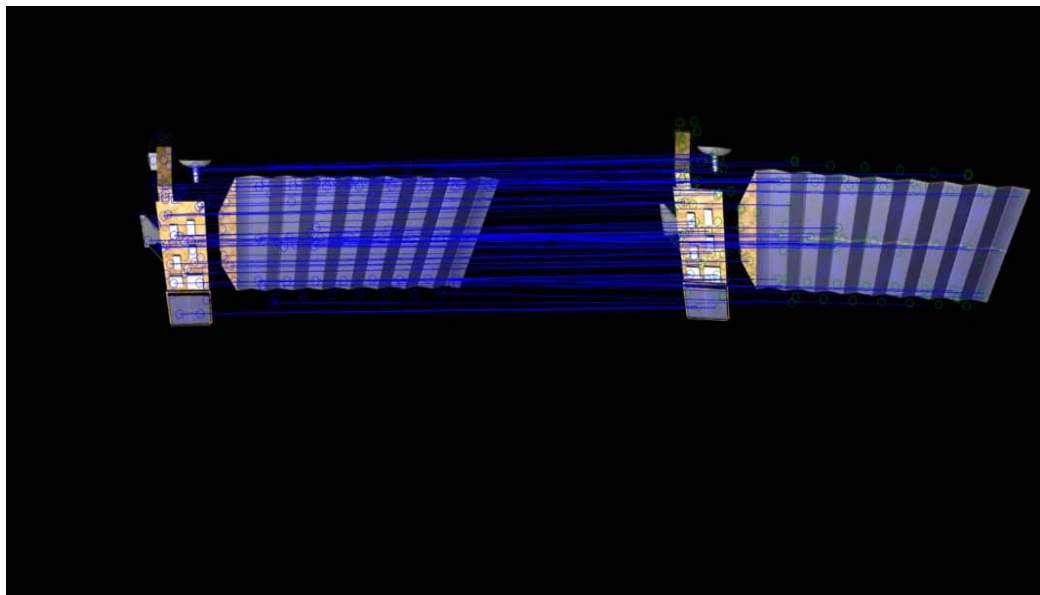
Figure 24. Correspondence Points Found Using SIFT
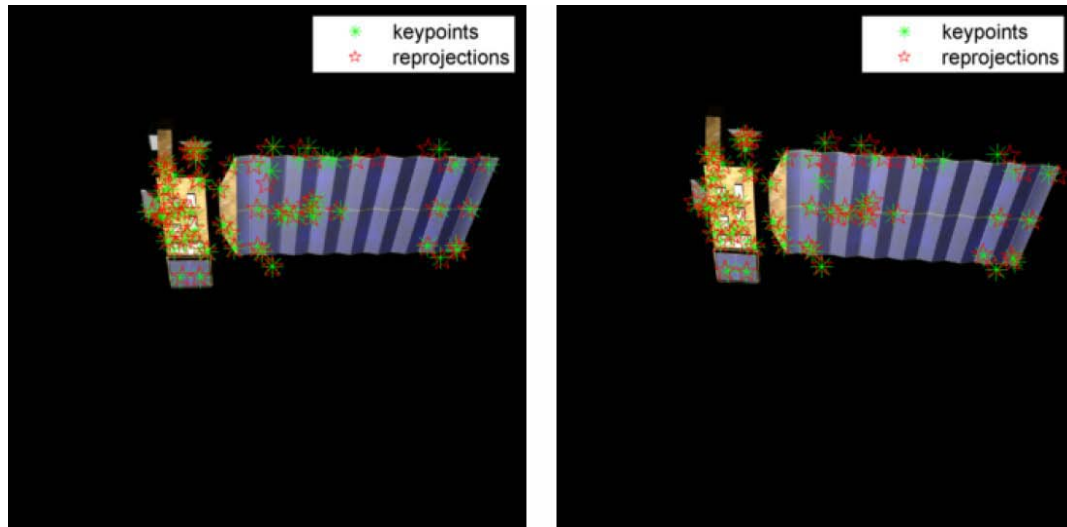
Figure 25. Automatic Correspondence Points - (a) Base Image Correspondence Points, (b) Comparison Image Correspondence Points
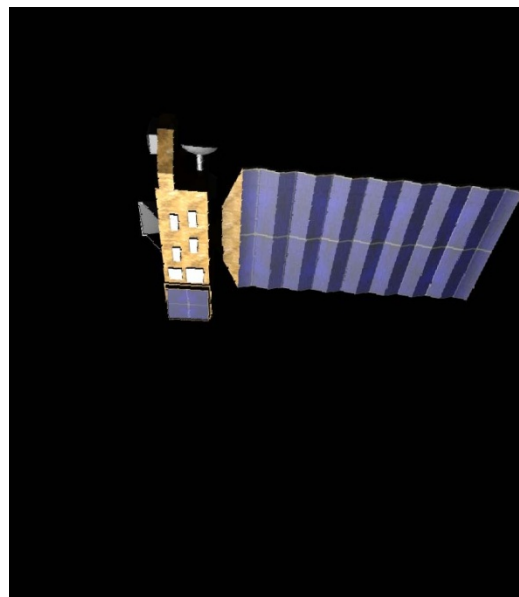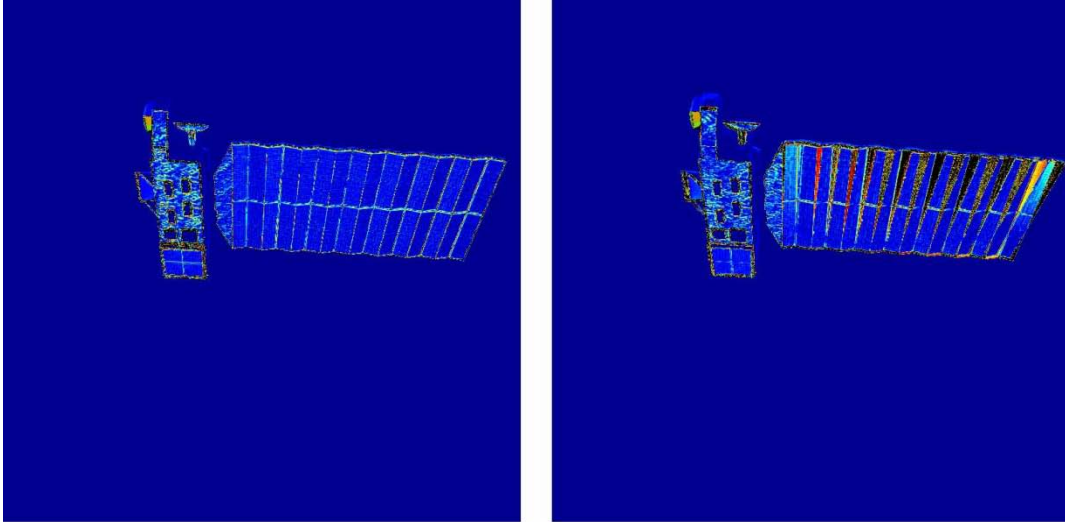

Figure 26. Warped Image

Figure 27. Comparison of Difference Images - (a) Direct Difference of Image I$_1$-I$_2$, (b) Warped Difference Image
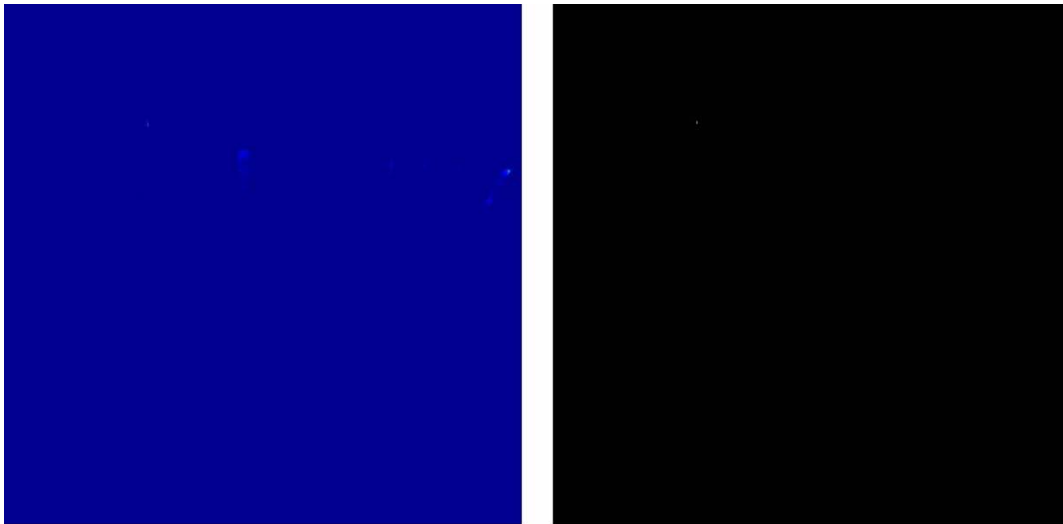
Figure 28. Removal of homography Errors

Note: See the above Figure 28 - (a) eroded warped image again appears nearly blank, but (b) with binary thresholding a small but significant white spot in the upper left corner indicates the true change

4.4   Pose-Based Change Detection

To evaluate the Pose-Based Change Detection technique, the performance of the optimal algorithm (4.1), the minimum-eigenvalue algorithm (4.2), and the textbook eight-point algorithm are compared by randomly generating ten noisy correspondence points which describe a

randomly generated pose. The pose estimate is compared to the pose which was originally used to generate the correspondence points. Recall that the rotation matrix from the first camera's coordinate system to the second camera's coordinate system is denoted by R, while the translation vector between the systems is denoted by T. The estimates of these quantities are denoted by R_{est} and T_{est}. The rotation error between R and R_{est} and the relative translation error between T and T_{est} are calculated for each case.

As can be seen in Figure 29, the minimum eigenvalue method outperforms the other algorithms when the standard deviation of the noise is greater than 0.002 normalized image coordinate units. Although the optimal algorithm is optimal in the sense that it minimizes 3D errors, it does not necessarily minimize R and T errors. For this reason, it is possible for the eight-point algorithm to outperform the optimal 3D algorithm. Although it would be expected that the optimal 3D algorithm would outperform the minimum-eigenvalue algorithm, since the minimum-eigenvalue algorithm is a simplified version of the optimal 3D algorithm, this is not the case. Both algorithms use a numerical search to find an optimal value, and do not have a closed form solution. Occasionally the numerical search fails to converge to the actual minimum value of the respective cost function. Due to the increased complexity of the search required by the optimal 3D algorithm, this algorithm fails to converge more frequently than the minimum-eigenvalue algorithm, resulting in its inferior performance.
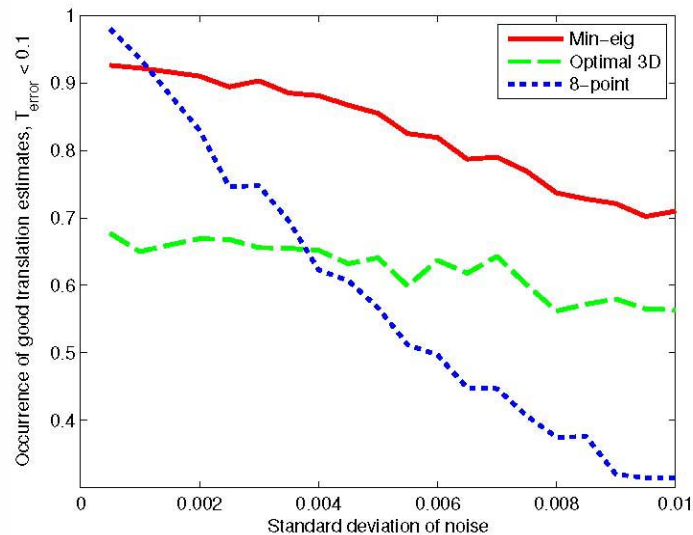
Figure 29. Performance of Pose Estimation Algorithms - (Top) Rotation Error as a Function of Noise, (Bottom) Translation Error as a Function of Noise

4.5   Simulation

To evaluate the performance of the algorithm, it is tested using the 3D model of the Aura satellite (a NASA mission to study Earth's ozone, air quality, and climate). Unlike the homography algorithm that only works for small rotation changes, this algorithm can be used for large changes in pose. Pose estimation algorithms are sensitive to correspondence point noise. To

ensure that the results are repeatable, correspondence points are generated using knowledge of the actual pose and the perspective transform to project points on the RSO into the images. Under these ideal circumstances, the pose estimation algorithm is capable of making estimates of the rotation accurate to within 0.005 degrees and estimates of the translation direction accurate to one part in 10,000. For this simulation, additive Gaussian noise with a standard deviation of 0.75 pixels is added to the x and y-components of the correspondence points.

The 800×800 pixel images that are used to test the algorithm are presented in Figure 30, and the correspondence points and their re-projections are shown in Figure 31

The pose is successfully estimated with an error of 0.74 degrees. This is the angle of rotation between the rotation matrices R and R_{est} (see [4]). Since the translation vector, T, is only known up to a scaling factor, an appropriate translation vector is computed such that the center of the satellite is in the center of the field of view of the camera with the estimated rotation. The rendered image with the estimated pose is shown in Figure 30(a). The difference image obtained by subtracting I_2 and I_3 is presented in Figure 32(b). Note that the area which is occupied by the box is highlighted in this image.

The difference image is eroded using a ball-shaped structuring element with a radius of eight pixels. A larger structuring element is used because the RSO occupies more of the image frame than in the images used to test the homography-based method. Otsu's method is used to convert eroded difference image into the change detection result. The eroded difference image and change detection result are given in Figure 33. Note that the algorithm detected the absence of the box in I_2. Also note that the pose-estimator based algorithm is able to cope with a much larger change in pose than the homography-based algorithm, because it has access to information on the areas of the RSO which are occluded in the base image.
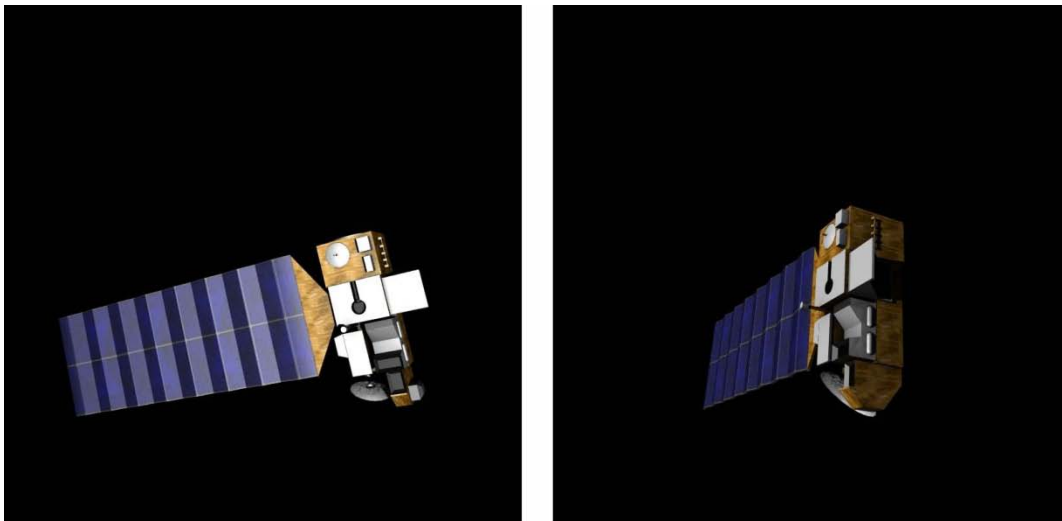
Figure 30. Test Images for Pose Algorithm - (a) Base Inspection I₁, (b) Comparison Inspection image, I₂
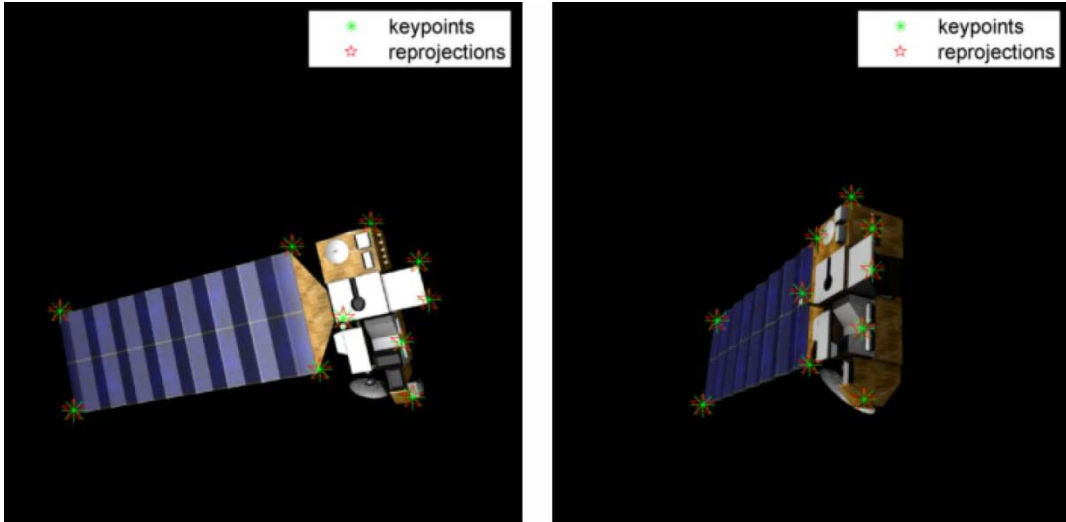
Figure 31. Pose Algorithm Correspondence Points - (a) Base Image Correspondence Points, (b) Comparison Image Correspondence Points
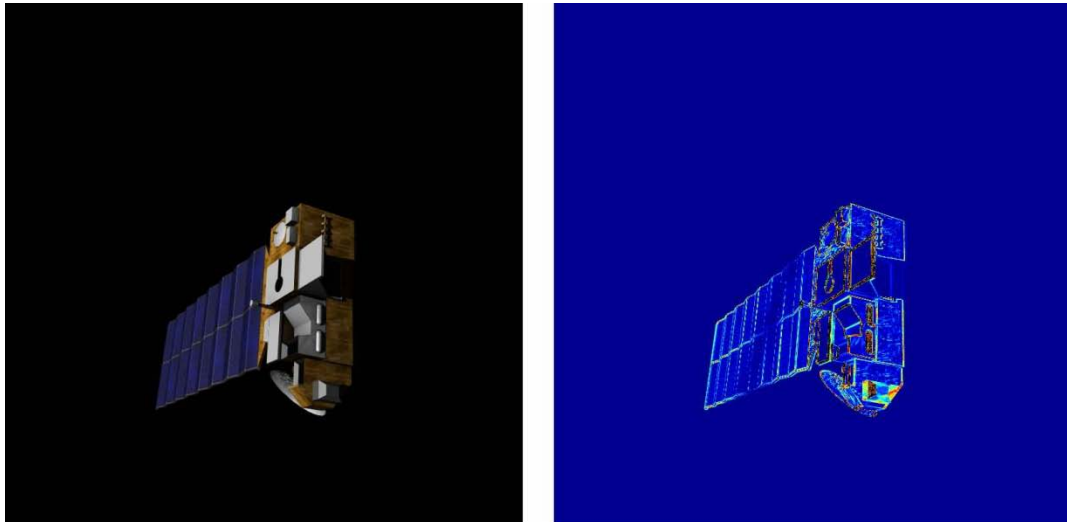
Figure 32. Rendering of difference images

Note: See Figure 32 above - (a) rendered image I_3, (b) difference image between I_2 and I_3. The added box can be easily detected as the colorful area. The colors here are generated directly by image subtraction, but the relation between color and error has not yet been established.
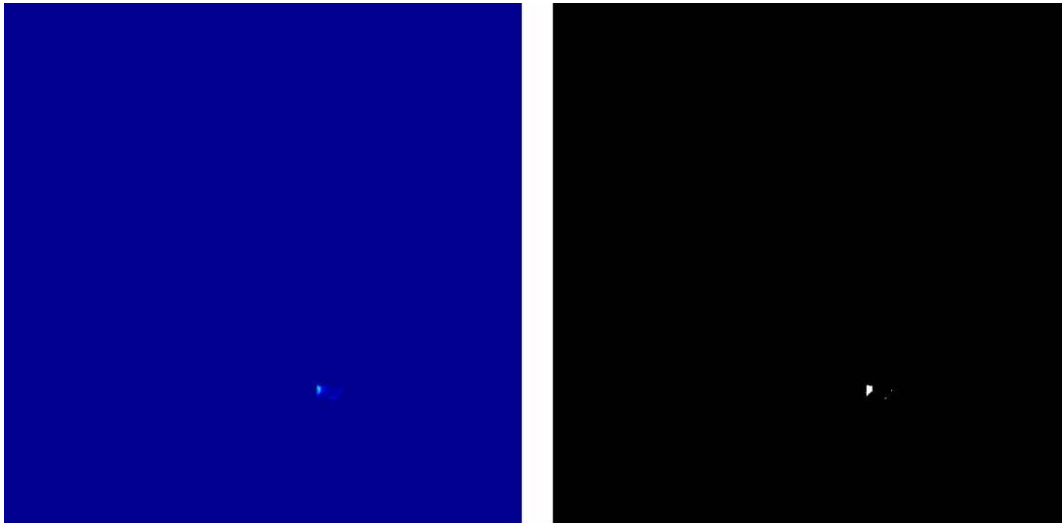
Figure 33. Processing of Difference Images

Note: See Figure 33 - - (a) eroded difference image shows only the added box, somewhat indistinctly in the lower right corner, but (b) the binary thresholding brings out the white spot indicating a change. This spot is easy to detect by computer search.

4.6   Angles-Only Navigation for Orbital Proximity Operations

The nominal flight path consists of an inspector satellite that is following a non-maneuvering RSO. The inspector is initially 406 m behind the RSO along the local-horizontal (v-bar) , 7 m above the RSO along the local-vertical (r-bar), and 15 m in the out-of plane/cross-track direction. To try to make the range observable, the inspector satellite fires thrusters every 75 seconds, alternating in the positive and negative cross-track directions for 15 and 16.5 seconds, respectively, to avoid a large net change in the position. The resulting thrust acceleration and flight path is shown Figure 34. The acceleration measurements in the cross-track direction are shown in green, and the acceleration measurements in the r-bar and v-bar directions are shown in red. This thruster firing pattern continues until the end of the simulation.

In this study, a trade analysis was performed corresponding to the good, average, and poor sensors suites listed in Figure 7. The result is an effective change in the accelerometer and LOS measurement's "signal to noise" as shown in Figure 35. The comparative performance of these suites is shown in Figure 36. The good sensor suite can resolve range to ±3 m, the average sensor suite resolves down to ±25 m and the poor sensor suite struggles to resolve range any better than ±160 m with non-linear effects causing the true error to leave the 3σ bound.   Overall, the good and average sensor suites are sufficiently accurate for range observability. However, the poor sensor suite is not sufficiently accurate to observe range reliably. This is an important result. It establishes a minimum accuracy requirement for accelerometers sensors.
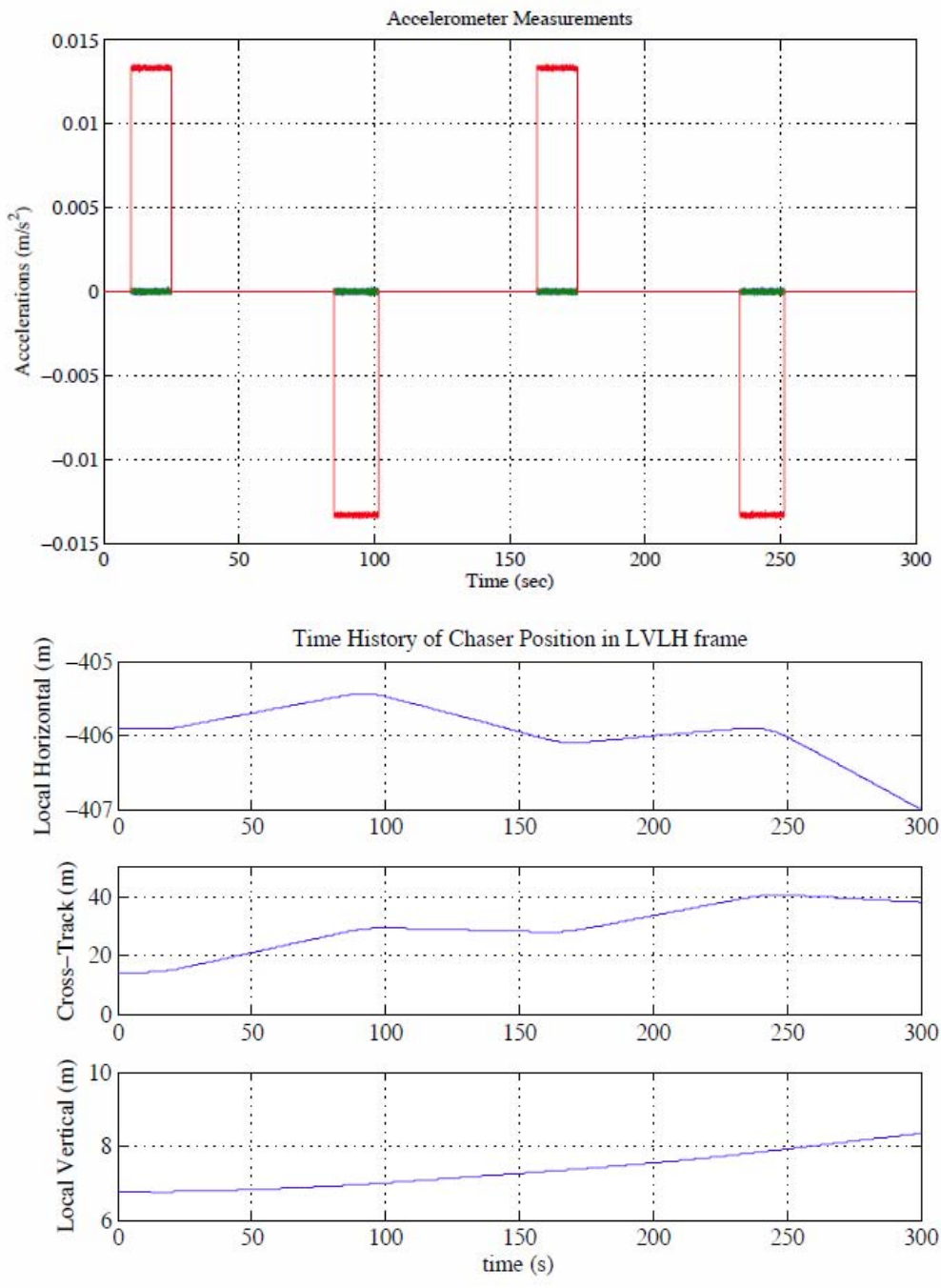
Figure 34. Nominal Flight Path (Top) Thrust Acceleration Profile, (Bottom) Trajectory in LVLH Coordinates
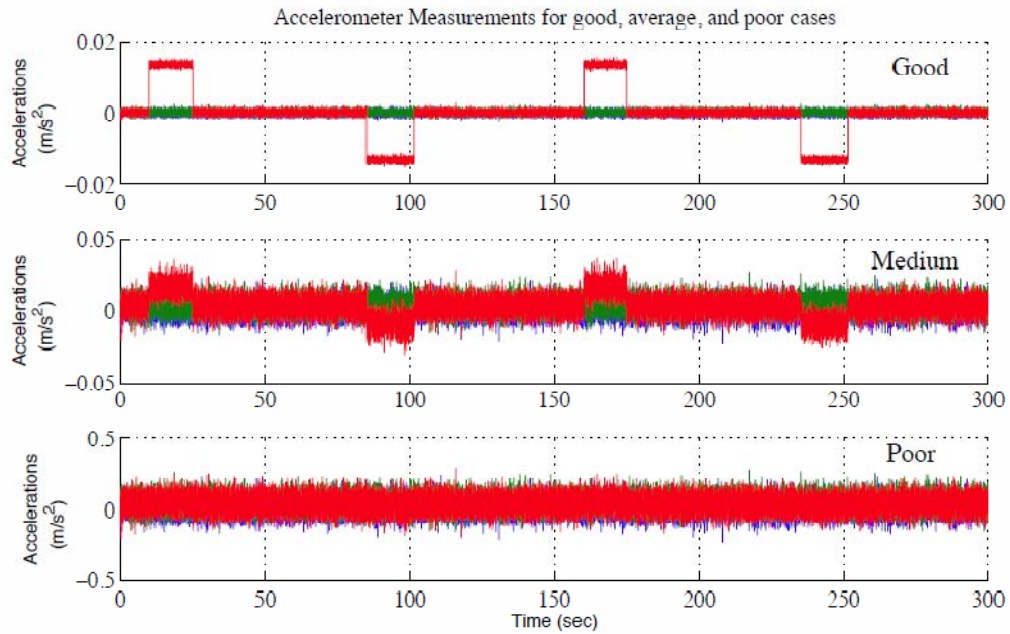
Figure 35. Accelerometer Measurements for Good, Average, and Poor Sensor Suites
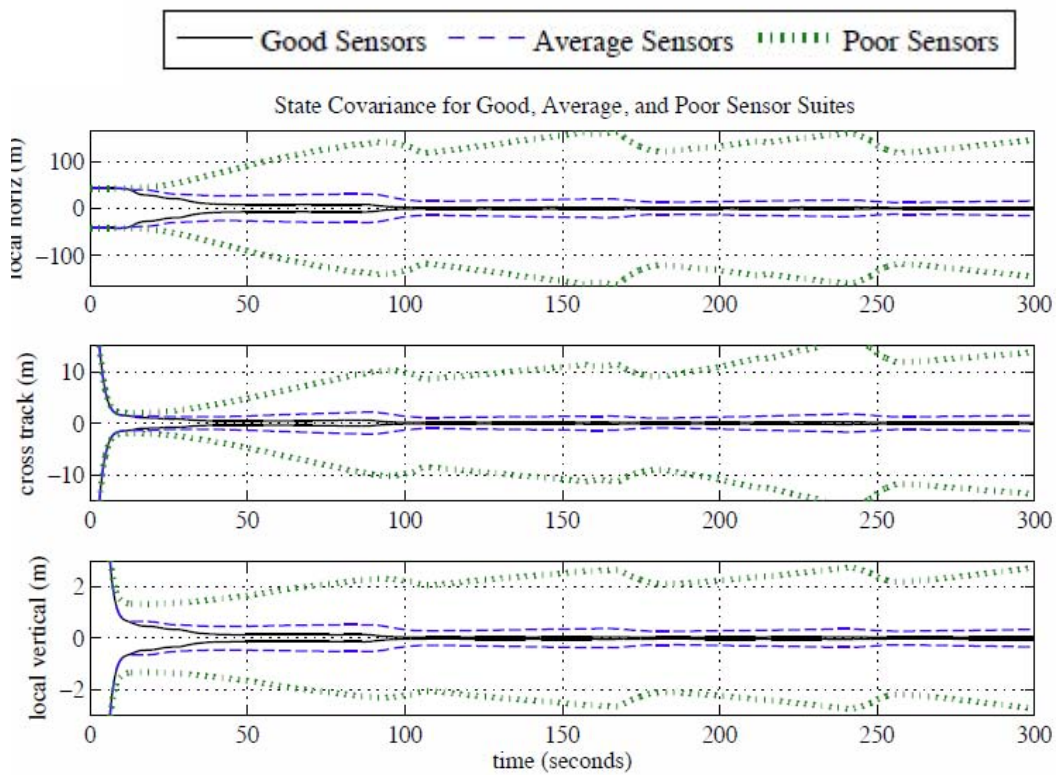
Figure 36. Effect of Sensor Suite Quality on Navigation Accuracy and Range Observability

4.7 Procedure for Determining Collision Probability during Proximity

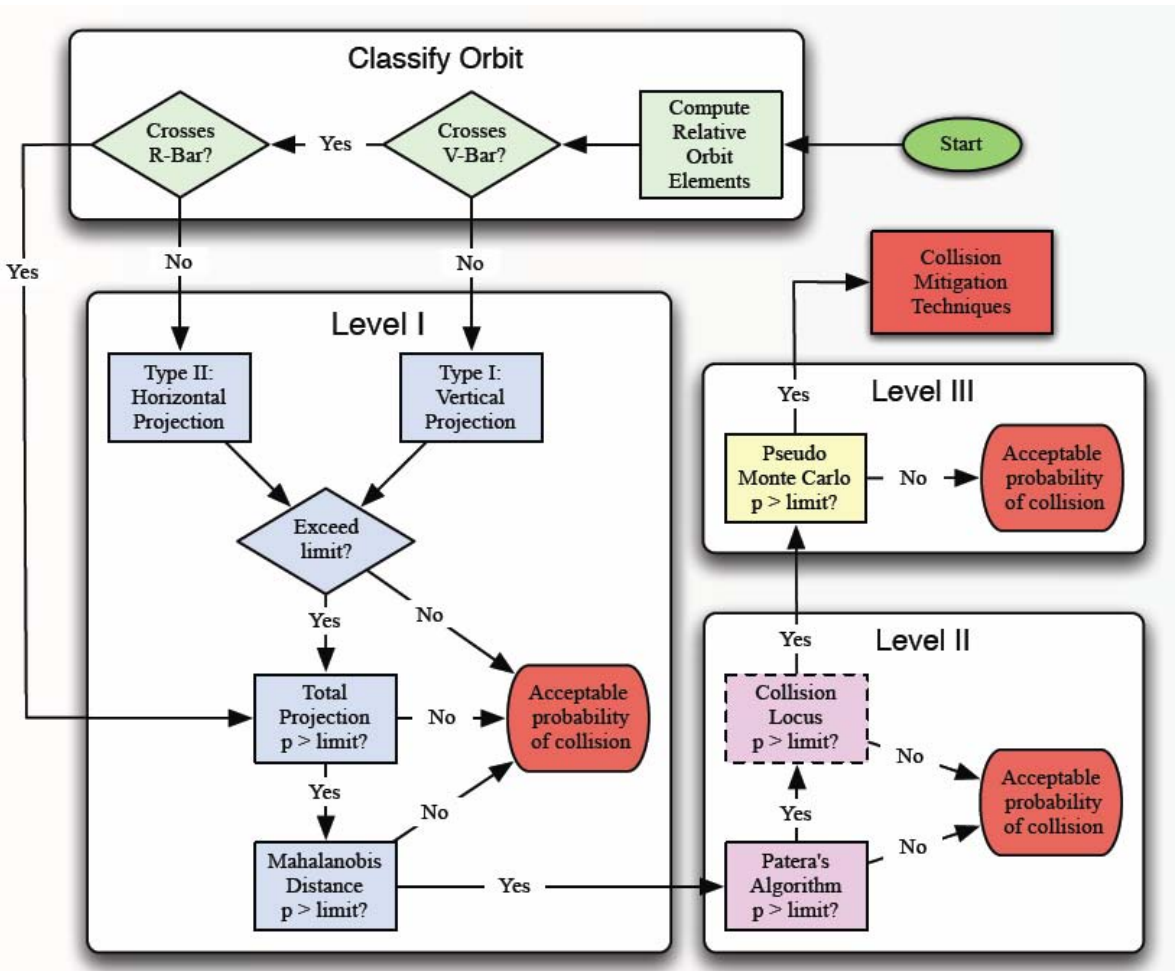A summary of the procedure that was developed is shown below in Figure 37.

Figure 37. Overview of the Collision Probability Prediction Algorithms

At this time unfortunately, only a minimal amount of data and results can be presented. Cases that have been run clearly show improved accuracy in the collision probability prediction as the algorithm progresses from one level to the next, and our preliminary results show that the results of one level bound the results of the next level. This gives us confidence that this approach is feasible. We hope the research in this area will continue.

5. CONCLUSIONS

5.1 Basic Mission Planning for LEO/GEO Space Operations

To obtain quality imagery of space objects autonomously, a collection of onboard mission and trajectory planners, GN&C algorithms, and image processing algorithms must be brought together and utilized in a closed-loop fashion to produce images that meet required metrics as defined by the customer. This research has taken the first step in identifying the procedures and algorithms that are required to accomplish this goal. Several of these have been developed and

implemented in closed-loop simulation including: 1) calculation of desired position and orientation to achieve better lighting conditions, 2) estimation of station-keeping maneuver Δv, and 3) and optimization of maneuver Δv for proximity operations. Future investigations and development will include maneuver triggers for robust dispersions control, trajectory predictors based on deterministic and linear covariance techniques, high-level fault detection, and robust safety procedures to insure that malfunctions do not result in collisions.

5.2   Optimal Inspection of Satellites Ensuring Lighting and Views of all Sides

 Methods for automatically planning the observation of RSOs at high resolution and low recurring cost have been developed. New metrics for predicting the quality of an image taken between two orbiting objects are developed for inclusion into the optimal planning process. The metric is aimed at predicting the observation quality a priori so that sensing plans can be autonomously formulated. Diffraction induced blur, line-of-sight, illumination, and lighting angle are included. In addition, new methods find an observation strategy guaranteeing that all RSOs are characterized on all of their important sides. The theory is also extended to emphasize the characterization of especially important RSOs, both at particular time intervals and relative to other RSOs. Simulation results confirm the viability of the technique on a variety of orbits.

5.3   Change Detection

Although homography estimation and pose estimation have been used by the computer vision community, the use of these techniques by a space borne change detection algorithm is believed to be novel. A literature search did not uncover any previous research which was specific to the problem of change detection in space-based inspection images. The use of morphological filters to remove model estimation errors has not been previously performed. In addition, two new pose estimation algorithms have been developed and tested, and they are shown to be especially robust to the high noise levels anticipated when inspecting satellites.

Both the homography-based and pose-based change detection algorithms are capable of recognizing changes to the appearance of the simulation images. The homography-based algorithm requires consistent lighting and can only operate on moderate changes in pose. Large changes in pose which expose a previously unseen side of the RSO are flagged as changes. The homography-based algorithm is much less sensitive to correspondence point noise than the pose-based algorithm.

The pose-based algorithm is capable of performing change detection under varying lighting conditions and large changes in pose, but is extremely sensitive to correspondence point noise. It does not require the assumption that the visible area of the RSO is a planar surface, which makes its change detection estimates more accurate in the absence of noise.

The minimum-eigenvalue algorithm is shown to produce usable pose estimates more frequently than the eight-point algorithm in the presence of correspondence point noise; therefore it is more suitable for use in space.

5.4 Angles-Only Navigation for Orbital Proximity Operations

The angles-only navigation analysis clearly shows that range observability is not an issue or problem provided that the onboard accelerometers and camera are of sufficient accuracy. If not, the range may be unobservable which may leave the inspector in a precarious position. The analysis also showed that further work is required to develop a controller and guidance system that will use less fuel by performing observability burns only when needed, and refraining from correcting position and velocity errors when the associated covariance is large.

5.5 Procedure for Determining Collision Probability during Proximity

The procedure we have developed for collision probability prediction during proximity operations is the first of its kind. Its usefulness is clear and its feasibility has been demonstrated. We are hopeful that this approach can over time be developed into real-time algorithm for onboard applications.

References

[1] D. Geller, J. McInroy, et al, "Autonomous Quality Space Imagery for LEO/GEO Space Operations," AIAA Conference on Guidance, Navigation, and Control, Honolulu, Hawaii, 2009.

[2] J. E. McInroy and L. Robertson, "Optimal Observation of Satellites Using Combined Measurements from Many Networked Observers Cooperatively Controlled by Human and Autonomous Means," AIAA Conference on Guidance, Navigation, and Control, (Toronto, Canada), August 2010.

[3] R. Buffington and J. E. McInroy, "Homography-Based Change Detection for Space Based Satellite Inspection," SPIE Conference on Defense, Security, and Sensing, (Orlando, FL), April 2011.

[4] R. Buffington and J. E. McInroy, "Change Detection for Visual Satellite Inspection Using Pose Estimation and Image Synthesis," SPIE Conference on Defense, Security, and Sensing, (Orlando, FL), April 2011.

[5] J. Schmidt, D. Geller, "Viability of Angles-Only Navigation for Orbital Rendezvous Operations," AIAA Conference on Guidance, Navigation, and Control, (Toronto, Canada), August 2010.

[6] J. Schmidt, "Analysis of Square-Root Kalman Filters for Angles-Only Orbital Navigation and the Effects of Sensor Accuracy on State Observability," MS Thesis, Utah State University, 2010.

[7] J. Irvine, "National Imagery Intelligence Rating Scale (NIIRS)," The Encyclopedia of Optical Engineering (R. Driggers, ed.), Marcel Dekker, 2003.

[8] J. Leachtenauer, "National Imagery Interpretability Rating Scales: Overview and Product Description," Proceedings of the American Society of Photogrammetry and Remote Sensing Annual Meetings, April 1996.

[9] J. C. Leachtenauer, W. Malila, J. M. Irvine, L. Colburn, and N. Salvaggio, "General Image-Quality Equation: GIQE," Applied Optics, Vol. 36, pp. 8322–8328, 1997.

[10] L. Maver, C. Erdman, and K. Riehl, "Imagery Interpretability Rating Scales," Digest of Technical Papers, International Symposium Society for Information Display, Vol. XXVI, pp. 117–120, 1995.

[11] M. Phillips, D. Geller, "Procedure for Determining Spacecraft Collision Probability During Orbital Rendezvous and Proximity Operations," AAS/AIAA Space Flight Mechanics Meeting, AAS 11-144, New Orleans, Feb. 2011.

[12] R. Patera, "General Method for Calculating Satellite Collision Probability," Journal of Guidance, Control, and Dynamics, Vol. 24, no. 4, July 2001.

DISTRIBUTION LIST

DTIC/OCP
8725 John J. Kingman Rd, Suite 0944
Ft Belvoir, VA 22060-6218   1 cy

AFRL/RVIL
Kirtland AFB, NM 87117-5776   2 cys

Official Record Copy
AFRL/RVSV/Frank Chavez   1 cy

(This page intentionally left blank)